United States
Environmental Protection
Agency

Office of Research and
Development
Washington DC 20460

EPA/600/R-99/095c
September 1999

EPA

An *In-Situ* Permeable Reactive Barrier for the Treatment of Hexavalent Chromium and Trichloroethylene in Ground Water:

Volume 3
Multicomponent Reactive Transport Modeling

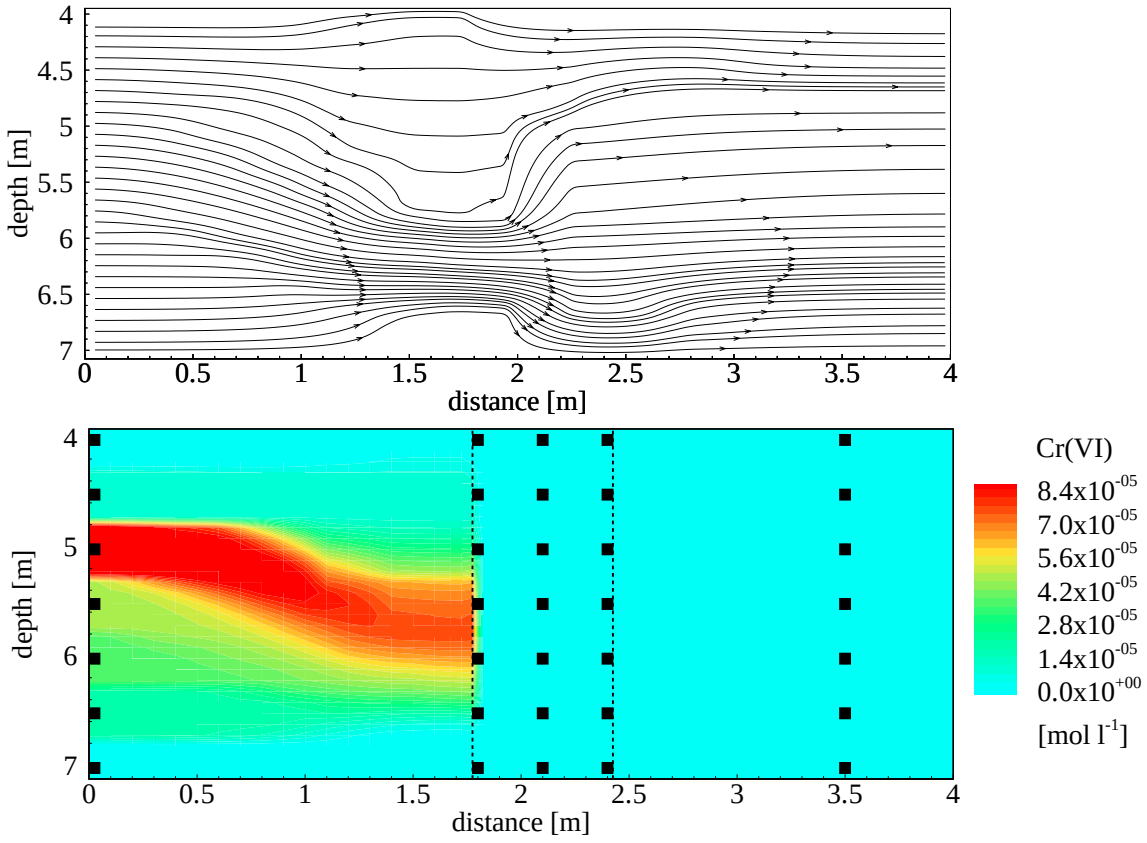

EPA/600/R-99/095c
September 1999

An *In-Situ* Permeable Reactive Barrier for the Treatment of Hexavalent Chromium and Trichloroethylene in Ground Water: Volume 3 Multicomponent Reactive Transport Modeling

David W. Blowes
K. Ulrich Mayer
Department of Earth Sciences
University of Waterloo
Waterloo, Ontario, Canada

Cooperative Agreement No. CR-823017

Project Officer
Robert W. Puls
Subsurface Protection and Remediation Division
National Risk Management Research Laboratory
Ada, OK 74820

National Risk Management Research Laboratory
Office of Research and Development
U.S. Environmental Protection Agency
Cincinnati, OH 45268

Notice

The U. S. Environmental Protection Agency through its Office of Research and Development partially funded and collaborated in the research described here under Cooperative Agreement No. CR-823017 to University of Waterloo. It has been subjected to the Agency's peer and administrative review and has been approved for publication as an EPA document. Mention of trade names or commercial products does not constitute endorsement or recommendation for use.

All research projects making conclusions or recommendations based on environmentally related measurements and funded by the Environmental Protection Agency are required to participate in the Agency Quality Assurance Program. This project was conducted under an approved Quality Assurance Project Plan. The procedures specified in this plan were used without exception. Information on the plan and documentation of the quality assurance activities and results are available from the Principal Investigator.

Foreword

The U.S. Environmental Protection Agency is charged by Congress with protecting the Nation's land, air, and water resources. Under a mandate of national environmental laws, the Agency strives to formulate and implement actions leading to a compatible balance between human activities and the ability of natural systems to support and nurture life. To meet these mandates, EPA's research program is providing data and technical support for solving environmental problems today and building a science knowledge base necessary to manage our ecological resources wisely, understand how pollutants affect our health, and prevent or reduce environmental risks in the future.

The National Risk Management Research Laboratory (NRMRL) is the Agency's center for investigation of technological and management approaches for reducing risks from threats to human health and the environment. The focus of the Laboratory's research program is on methods for the prevention and control of pollution to air, land, water, and subsurface resources; protection of water quality in public water systems; remediation of contaminated sites and ground water; and prevention and control of indoor air pollution. The goal of this research effort is to catalyze development and implementation of innovative, cost-effective environmental technologies; develop scientific and engineering information needed by EPA to support regulatory and policy decisions; and provide technical support and information transfer to ensure effective implementation of environmental regulations and strategies.

Environmental scientists are generally familiar with the concept of barriers for restricting the movement of contaminant plumes in ground water. Such barriers are typically constructed of highly impermeable emplacements of materials such as grouts, slurries, or sheet pilings to form a subsurface "wall." The goal of such installations is to eliminate the possibility that a contaminant plume can move toward and endanger sensitive receptors such as drinking water wells or discharge into surface waters. Permeable reactive barrier walls reverse this concept of subsurface barriers. Rather than serving to constrain plume migration, permeable reactive barriers (PRBs) are designed as preferential conduits for the contaminated ground water flow. A permeable reactive subsurface barrier is an emplacement of reactive materials where a contaminant plume must move through it as it flows, typically under natural gradient, and treated water exits on the other side. The purpose of this document is to provide detailed design, installation and performance monitoring data on a full-scale PRB application which successfully remediated a mixed waste (chromate and chlorinated organic compounds) ground-water plume. It was also the first full-scale installation of this technology to use a trencher to install a continuous reactive wall to intercept a contaminant plume. The information will be of use to stakeholders such as implementors, state and federal regulators, Native American tribes, consultants, contractors, and all other interested parties. There currently is no other site which has used this innovative technology and reported on its performance to the extent detailed in this report. It is hoped that this will prove to be a very valuable technical resource for all parties with interest in the implementation of this innovative, passive, remedial technology.

Clinton W. Hall, Director
Subsurface Protection and Remediation Division
National Risk Management Research Laboratory

Abstract

Reactive transport modeling has been conducted to describe the performance of the permeable reactive barrier at the U.S. Coast Guard Support Center near Elizabeth City, N.C. The reactive barrier was installed to treat groundwater contaminated by hexavalent chromium and chlorinated organic solvents. The conceptual model of the Elizabeth City site described in Volumes 1 and 2 of this document series (Blowes et al., 2000) provide the basis for the modeling study. The multicomponent reactive transport model MIN3P was used for the simulations. The essential reactions contained in the conceptual model are aqueous complexation reactions, combined reduction-corrosion reactions between the treatment material zero-valent iron and the contaminants or other electron acceptors dissolved in the ambient groundwater and the precipitation of secondary minerals within the reactive barrier. The simulations have been carried out along a cross-section through the barrier that corresponds to a transect of the monitoring network. One- and two-dimensional simulations were conducted. The one-dimensional simulations were carried out along a zone of preferential flow, which conveys the most pronounced Cr(VI)-contamination. The model has been calibrated using field data, laboratory data and reaction rates reported in the literature. The two-dimensional simulations were conducted based on hydraulic conductivities determined from slug-tests. These simulations allow an evaluation of the impact of preferential flow on the treatment of the contaminants and secondary reactions. The model results provide estimates of the potential effects of the consumption of zero-valent iron and the precipitation of secondary minerals on the long-term efficiency of the treatment system.

Contents

Foreword iii
Abstract v
Tables viii
Figures ix
Introduction 1
Description of MIN3P 1
Conceptual Model 5
Definition of Reaction Network 5
    Complexation Reactions 5
    Reduction-corrosion Reactions 5
    Formation of Secondary Minerals in Treatment Zone 6
    pH and Eh-buffering Downgradient of Barrier 6
        pH-buffering 6
        Eh-buffering 7
Solution Domain and Model Parameters 8
    Spatial Discretization 8
    Physical Parameters and Hydraulic Conductivity Distribution 8
    Mineralogical Parameters 9
    Boundary and Initial Chemical Composition of Ground Water 9
Calibrated Rate Constants 9
Results and Discussion 10
    One-dimensional Simulations 11
        Removal of Contaminants 11
        Reduction of Electron Acceptors 11
        Selected Cation Concentrations 11
        pH and Eh 12
        Discussion of Reaction Mechanisms 12
        Corrosion of Zero-valent Iron 13
        Precipitation of Secondary Minerals 13
        Long Term Efficiency 13
    Two-dimemsional Simulations 14
        Ground-water Flow 14
        Removal of Contaminants 14
        pH and Eh 14
        Sulfate Reduction 15
Conclusions 15
References 16

Tables

Table 1. Complexation reactions and equilibrium constants 19
Table 2. Reaction stoichiometries of reduction-corrosion reactions 21
Table 3. Secondary minerals in reactive barrier and corresponding equilibrium constants 22
Table 4. Physical parameters for aquifer and reactive barrier material 22
Table 5. Initial mineral volume fractions in reactive barrier and aquifer 22
Table 6. Reactive surface area estimates for zero iron-valent (field installation) 22
Table 7. Reactive surface area estimates for *E*h buffer minerals 23
Table 8. Input concentrations at boundary located upgradient of reactive barrier, Transect 2, 21-1 - 21-4 23
Table 9. Input concentrations at boundary located upgradient of reactive barrier, Transect 2, 21-5 - 21-7 24
Table 10. Reaction processes affecting component concentrations 25
Table 11. Rate constants for reduction-corrosion reactions 26
Table 12. Calibrated effective rate constants for secondary mineral formation 26
Table 13. Estimated rate constants for reductive dissolution reactions 26

Figures

Figure 1. Configuration of reactive barrier and approximate location of chromium plume, from *Bennett* [1997] 28
Figure 2. Monitoring network, from *Bennett* [1997] 28
Figure 3. Conceptual model for reactive barriers comprised of zero-valent iron, from *Bennett* [1997] 29
Figure 4. Solution domain including location of barrier and monitoring points along Transect 2 29
Figure 5. Spatial discretization of two-dimensional solution domain 30
Figure 6. Hydraulic conductivity distribution in two-dimensional solution domain, modified from *Bennett* [1997] 30
Figure 7. Contaminant concentrations after *t* = 240 days: a) chromium, b) organics - one-dimensional simulation 31
Figure 8. Redox couple concentrations after *t* = 240 days: a) nitrate/ammonia, b) sulfate/sulfide - one-dimensional simulation 31
Figure 9. Selected cation concentrations after *t* = 240 days - one-dimensional simulation 32
Figure 10. pH and *E*h after t = 240 days - one-dimensional simulation 32
Figure 11. Iron corrosion rates in reactive barrier after *t* = 240 days 33
Figure 12. Secondary mineral volume fractions in reactive barrier after *t* = 240 days 33
Figure 13. Long term effect of iron corrosion and secondary mineral formation 34
Figure 14. Streamlines in two-dimensional solution domain 34
Figure 15. Hexavalent and trivalent chromium concentrations and $CrOH_3$(am) volume fractions after *t* = 2 years 35
Figure 16. TCE, cis-1,2 DCE and VC concentrations after *t* = 2 years 36
Figure 17. pH and *E*h distribution after *t* = 2 years 37
Figure 18. Sulfate and sulfide concentrations and mackinawite volume fractions after t = 2 years 38

Introduction

This report describes the application of the multicomponent reactive solute transport model MIN3P [*Mayer,*1999], using one- and two-dimensional reactive transport simulations to model treatment of contaminated ground water by an *in-situ* permeable reactive barrier. The modeling study is based on the conceptual model developed by *Bennett* [1997] for the barrier installation at the U.S. Coast Guard Support Center near Elizabeth City, North Carolina. The reactive barrier was designed to treat the ambient ground water, which is contaminated with hexavalent chromium, and trichloroethylene (TCE) and its degradation products. The technology for this barrier was developed and is atented by the University of Waterloo. The chromium contamination originates from a plating facility located in Hangar 79 (Figure 1). The contaminated ground water is moving north, and is intercepted by the reactive barrier before entering the Pasquotank River. Chromium concentrations upgradient of the reactive barrier exceed 1 mg L^{-1} and locally reach up to 5 mg L^{-1} [*Bennett*,1997; *Blowes et al.*, 2000]. A larger plume containing chlorinated organic compounds emanating from the vicinity of Hangar 79 and is also treated by the barrier [*Bennett*,1997; *Blowes et al.*, 2000]. The barrier is comprised of granular iron and remediates the ground water by reduction of hexavalent chromium and subsequent precipitation in the form of chromium containing hydroxides [*Bennett*, 1997; *Blowes et al*.,1999]. Trichloroethylene and its major degradation products cis-1,2 dichloroethylene (cis-1,2 DCE) and vinyl-chloride (VC) are converted to non-toxic hydrocarbons by reductive elimination and hydrogenolysis [*Bennett*, 1997; *Blowes et al*, 1997]. An extensive field monitoring program was initiated at the site [*Bennett*,1997; *Blowes et al.*, 2000]. Multi-level sampling wells facilitate a detailed description of the hydrogeology of the aquifer and the geochemical conditions upgradient, within and downgradient of the treatment system along three transects (Figure 2). Only limited data regarding the mineralogical composition of the aquifer and the treatment material were available when conducting the simulations. Assumptions made with respect to the mineralogy are compared to the results of the mineralogical analyses carried out by *Palmer* [1999].

In the following section the formulation of the numerical reactive transport model MIN3P is introduced. The conceptual model developed by *Bennett* [1997], which describes the controlling transport and reaction processes in the treatment system and forms the basis for this modeling study, is presented. The reaction network for the numerical analysis is defined based on this conceptual model. One- and two-dimensional reactive transport modeling is conducted to describe the geochemical evolution of ground water along Transect 2 (Figure 2). Changes of the geochemical composition of the reactive mixture and the aquifer material downgradient of the barrier are also addressed. An investigation of processes potentially affecting the long-term performance of the reactive barrier is carried out. The modeling results are discussed with a focus on the expected efficiency and longevity of the treatment system. The effect of preferential flow on the quality of the treatment for the various contaminants is investigated.

Description of MIN3P

The model MIN3P was developed by *Mayer* [1999] as a general purpose multicomponent reactive transport model facilitating the simulation of reactive solute transport in variably-saturated media. The governing equations presented here focus on the formulation for saturated porous media only, because the current modeling study does not include unsaturated conditions. In this case, the mass conservation equations for reactive transport consist of relationships describing advective-dispersive transport of aqueous species under the influence of homogeneous and heterogeneous geochemical reactions. A global implicit formulation [*Steefel and Lasaga*,1994] is used, in which case the geochemical reaction expressions are directly substituted into the transport equations. Reaction processes considered are aqueous complexation, oxidation-reduction, ion-exchange, and dissolution-precipitation reactions. The formulation of the model is based on a partial equilibrium approach [*Lichtner*, 1985; *Sevougian et al*., 1993; *Steefel and Lasaga*, 1994], which contains geochemical equilibrium reactions as well as homogeneous and heterogeneous kinetic reactions. The global mass conservation equation for the components A_j^c are defined by:

$$\frac{\partial}{\partial t}\left[\phi C_j^c\right]+\sum_{i=1}^{N_x}\nu_{ij}^x\frac{\partial}{\partial t}\left[\phi C_i^x\right]+\sum_{i=1}^{N_s}\nu_{ij}^s\frac{\partial C}{\partial t}+\nabla\cdot\left[\boldsymbol{v}_a C_j^c\right]-\nabla\cdot\left[\phi\mathbf{D}_a\nabla C_j^c\right]$$
$$+\sum_{i=1}^{N_x}\nu_{ij}^x\nabla\cdot\left[\boldsymbol{v}_a C_i^x\right]-\sum_{i=1}^{N_x}\nu_{ij}^x\nabla\cdot\left[\phi\mathbf{D}_a\nabla C_i^x\right]-Q_j^{a,m}-Q_j^{a,a}=0 \qquad j=1,N_c \tag{1}$$

where t defines time and ϕ is porosity. The concentrations of the dissolved species are defined by C_j^c (concentrations of components as species in solution) and C_i^x (concentrations of complexed species). C_i^s defines the concentrations of the ion-exchanged species. N_x defines the number of aqueous complexes, and N_s identifies the number of ion-exchanged species in the system. v_{ij}^x and v_{ij}^s are the stoichiometric coefficients of the components in the complexed species and ion-exchanged species. The source-sink terms $Q_j^{a,m}$ and $Q_j^{a,a}$ define the gain or loss of mass for a component due to kinetically-controlled dissolution-precipitation reactions, and kinetically-controlled intra-aqueous reactions, respectively. v_a defines the Darcy velocity.

The hydrodynamic dispersion coefficient D_a is given by [*Bear*, 1972; *Unger et al.*, 1995]

$$\phi \mathbf{D}_{a,kl} = (\alpha_l - \alpha_t)\frac{\boldsymbol{v}_{a,k}\boldsymbol{v}_{a,l}}{|\boldsymbol{v}_a|} + \alpha_t |\boldsymbol{v}_a| \delta_{kl} + \phi \tau_a D_a^* \delta_{kl} \tag{2}$$

where k and l define the spatial coordinates, α_l is the longitudinal and α_t is the transverse dispersivity of the porous medium, $|\boldsymbol{v}_a|$ is the magnitude of the Darcy flux in the aqueous phase, D_a^* is an averaged free liquid diffusion coefficient used for all dissolved species [$m^2\ s^{-1}$] and τ_a is the tortuosity of the medium [-]. The formulation of the dispersion tensor is based on the implementation by *Unger et al.*[1995] and allows for different transverse dispersivities in horizontal and vertical directions, which can be defined as α_{th} and α_{tv}. δ_{kl} defines the Kronecker delta.

The governing equation 1 for reactive transport can be simplified by expressing the concentrations of all aqueous species in terms of total aqueous component concentrations T_j^a [mol L^{-1} water] [*Kirkner and Reeves*, 1988; *Steefel and Lasaga*, 1994; *Lichtner*, 1996]:

$$T_j^a = C_j^a + \sum_{i=1}^{N_x} v_{ij}^x C_i^x \tag{3}$$

A corresponding relationship can be defined for the adsorbed species in terms of total sorbed component concentrations T_j^s [mol L^{-1} bulk]:

$$T_j^s = \sum_{i=1}^{N_s} v_{ij}^s C_i^s \tag{4}$$

Equation 1 can then be written as:

$$\frac{\partial}{\partial t}[\phi T_j^a] + \frac{\partial T_j^s}{\partial t} + \nabla \cdot [v_a T_j^a] - \nabla \cdot [\phi D_a \nabla T_j^a] - Q_j^{a,m} - Q_j^{a,a} = 0 \qquad j = 1, N_c \tag{5}$$

To complete the system of governing equations, an additional set of mass conservation equations has to be defined, which describes the change of mineral quantities over time [*Steefel and Lasaga*, 1994]:

$$\frac{d\varphi_i}{dt} = 10^{-3} V_i^m R_i^m \qquad i = 1, N_m \tag{6}$$

where φ_i is the volume fraction of the i^{th} mineral [m^3 mineral m^{-3} bulk], $\boldsymbol{V}_i^m$ is the molar volume of the i^{th} mineral [$cm^3\ mol^{-1}$], $\boldsymbol{R}_i^m$ is the overall dissolution-precipitation rate for the i^{th} mineral [mol L^{-1} bulk s^{-1}] and 10^{-3} is a unit conversion factor [L cm^{-3}].

The nonlinear mass conservation equation 5 has a form similar to those given by *Kirkner and Reeves* [1988], *Steefel and Lasaga* [1994] and *Lichtner* [1996] and is written in terms of total aqueous and sorbed component concentrations with the components as species in solution as primary unknowns, the units of each term in equation 5 is [mol L^{-1} bulk s^{-1}]. Equation 6 has the units [m^3 mineral m^{-3} bulk s^{-1}].

The formulation for activity corrections for all dissolved species has been adopted from the thermodynamic equilibrium model MINTEQA2 [*Allison et al.*, 1991]. Activity coefficients γ_i^d for the charged dissolved species A_i^d, where A_i^d can be either a component as species in solution or an aqueous complex, are calculated based on the modified Debye-Hückel equation, given by

$$\log \gamma_i^d = \frac{-A_d Z_i^2 I^{1/2}}{1 + B_d a_i I^{1/2}} + b_i I \tag{7}$$

where A_d and B_d are constants, a_i is the ion size parameter, b_i is an ion specific parameter that accounts for the decrease in solvent concentration in concentrated solutions. If a_i is available, but not b_i, equation 7 is used with $b_i = 0$. The Davies equation is used as an approximation when the parameter a_i cannot be provided:

$$\log \gamma_i^d = -A_d Z_i^2 \left[\frac{I^{1/2}}{1 + I^{1/2}} - 0.24I \right] \tag{8}$$

The activity coefficients for all neutral species excluding water are calculated according to:

$$\log \gamma_i^d = 0.1I \tag{9}$$

while the activity correction for water is defined by:

$$\gamma_{H_2O} = 1 - 0.017 \sum_{i=1}^{N_d} C_i^d \tag{10}$$

A stoichiometric relationship for the dissociation of the aqueous complex A_i^x into components as species in solution can be formulated as:

$$A_i^x \leftrightarrow \sum_{i=1}^{N_c} v_{ij}^x A_i^c \qquad i = 1, N_x \tag{11}$$

where v_{ij}^x is the stoichiometric coefficient of the j^{th} component in the i^{th} aqueous complex A_i^x. Equilibrium complexation reactions can be described by the law of mass action. The set of algebraic equations, describing the dissociation of aqueous complex A_i^x into components as species in solution can be written as:

$$C_i^x = (K_i^x \gamma_i^x)^{-1} \prod_{j=1}^{N_c} (\gamma_j^c C_j^c)^{v_{ij}^x} \qquad i = 1, N_x \tag{12}$$

where K_i^x is the equilibrium constant for the dissociation of the i^{th} aqueous complex into components as species in solution, γ_i^x is the activity coefficient for the i^{th} aqueous complex and γ_j^c is the activity coefficient for the j^{th} component as species in solution. Equation 12 can also be used for equilibrium-controlled homogeneous oxidation-reduction reactions.

Complexation and oxidation-reduction reactions can also be described as kinetically-controlled reactions. The reaction stoichiometry for a kinetically-controlled intra-aqueous reaction can be expressed in terms of components as species in solution [*Lichtner*, 1996b]

$$0 \leftrightarrow \sum_{j=1}^{N_c} v_{ij}^a A_j^c \qquad i = 1, N_a \tag{13}$$

where v_{ij}^a are the stoichiometric coefficients of the species participating in the reaction, and N_a defines the number of kinetically-controlled intra-aqueous reactions.

The model includes a general formulation for kinetically-controlled reactions. The reaction rate for an intra-aqueous reaction can be expressed as a function of the forward and backward rate constants k_k^{af} and k_k^{ab}, the activities of the components as species in solution and aqueous complexes a_j^c and a_i^x, total aqueous component concentrations and the equilibrium constant of the reaction. A rate expression in symbolic form for the k^{th} kinetically-controlled intra-aqueous reaction can be written as

$$R_k^a = f\left(k_k^{af}, k_k^{ab}, a_j^c, a_i^x, T_j^a, K_k^a\right) \tag{14}$$

where k_k^{af} and k_k^{ab} are the rate constants for the forward and backward reactions respectively. Mass loss or gain for a particular component enters the global mass conservation equation through the source-sink term $Q_j^{a,a}$, which is defined by:

$$Q_j^{a,a} = \phi \sum_{i=1}^{N_a} \nu_{ij}^a R_i^a \qquad j = 1, N_c \tag{15}$$

where the contributions of the various reactions rates were scaled to express the source-sink term in the units of the global mass conservation equations [mol L^{-1} bulk s^{-1}].

The model allows the consideration of ion-exchange reactions in terms of the Gapon- and Gaines-Thomas conventions [Appelo and Postma, 1993]. A general stoichiometric relationship based on the Gaines Thomas model can be written as

$$A_i^s \leftrightarrow \nu_i^s A_k^s \sum_{j=1}^{N_c} \nu_{ij}^s A_j^c \qquad i = 1, N_s \tag{16}$$

where ν_i^s is the stoichiometric coefficient of the ion-exchanged species A_k^s in the i^{th} ion exchange reaction, which is defined by the ratio of the charge of the two participating cations. ν_{ij}^s are the stoichiometric coefficients of the components and N_s defines the number of the ion-exchanged species. Based on the stoichiometry defined in reaction equation 16, the law of mass action can be used to obtain a relationship that defines the activities of the ion-exchanged species A_i^s in terms of equivalent fractions

$$\beta_i = \left(K_i^s\right)^{-1} \left(\beta_k\right)^{\nu_i^s} \prod_{j=1}^{N_c} \left(\gamma_j^c C_j^c\right)^{\nu_{ij}^s} \qquad i = 1, N_s,\ i \neq k \tag{17}$$

where $ß_i$ and $ß_k$ are the activities of the ion-exchanged species A_i^s and A_k^s [meq meq^{-1}] and K_i^s is the selectivity coefficient for the i^{th} ion-exchange reaction. The actual concentrations of the ion-exchanged species can be obtained by applying the conversion:

$$C_i^s = \frac{\rho_b}{100} CEC (Z_i^s)^{-1} \beta_i \tag{18}$$

where C_i^s is the concentration of the ion-exchanged species A_i^s [mol L^{-1} bulk], ρ_b is the dry bulk density of the porous medium [g solid cm^{-3} bulk] and *CEC* defines the cation exchange capacity [meq $(100g)^{-1}$ solid]. The factor 100 provides the conversion [g $(100g)^{-1}$].

A general stoichiometric relationship, which describes the congruent dissolution or precipitation of a mineral in terms of components as species in solution can be written as:

$$A_i^m \leftrightarrow \sum_{j=1}^{N_m} \nu_{ij}^m A_j^c \qquad i = 1, N_m \tag{19}$$

where A_i^m defines the i^{th} mineral, ν_{ij}^m are the stoichiometric coefficients of the components as species in solution comprising the mineral A_i^m, and N_m defines the number of minerals actively participating in dissolution-precipitation reactions.

General rate expressions for surface- and transport-controlled dissolution-precipitation reactions can be written as a function of the dissolution and precipitation rate constants (k_k^{md} and k_k^{mp}), the diffusion coefficients of the primary reactant species through a protective surface layer (D_k^m), geometric parameters such as the representative mineral particle radius (r_k^p), the thickness of a protective surface layer (r_k^r), and the reactive mineral surface area (S_k). The rate expression will depend in addition on the activities of the components as species in solution and aqueous complexes, total aqueous component concentrations, and the equilibrium constant of the reaction (K_k^m). The rate expression for the dissolution of the k^{th} mineral phase can be expressed in symbolic form as:

$$R_k^m = f(k_k^{md}, k_k^{mp}, D_k^m, r_k^p, r_k^r, S_k, a_j^c, a_i^x, T_j^a, K_k^m) \tag{20}$$

The formulation also allows the consideration of parallel reaction pathways. The source-sink term describing the production or consumption of components due to dissolution-precipitation reactions can be written as:

$$Q_j^{a,m} = -\sum_{i=1}^{N_m} \nu_{ij}^m R_i^m \qquad j = 1, N_c \tag{21}$$

Conceptual Model

The conceptual model developed through field studies at the Elizabeth City site [*Bennett*, 1997; *Blowes et al.*, 2000] was subdivided into three zones: upgradient aquifer, the reactive barrier, and the aquifer downgradient of the barrier (Figure 3). The zone located upgradient of the treatment system was termed the “contaminated zone.” The contaminated ground water in this zone has been in contact with aquifer material for a considerable amount of time, and dissolved species are either in equilibrium with the aquifer material, or reactions are kinetically limited. Dissolved species are transported more or less conservatively through this zone by advective and dispersive transport processes [*Bennett*, 1997].

The second zone is located within the reactive barrier and was termed the “treatment zone.” In this zone, the contaminants are transformed by reduction and immobilized by subsequent precipitation [*Bennett*, 1997; *Blowes et al.*, 2000]. A number of secondary reactions occur simultaneously in the treatment zone. Other oxidized species, such as dissolved oxygen, nitrate, sulfate, dissolved inorganic carbon, dissolved organic carbon and water are reduced either directly by zero-valent iron or by dissolved reduced species; for example, hydrogen gas [*Bennett*, 1997]. Isotopic data indicates that sulfate reduction may be microbially-mediated. These reduction reactions lead to the corrosion of zero-valent iron, which serves as the ultimate electron donor. Major reaction products of these corrosion reactions are ferrous or ferric iron and dissolved gases. The combined effect of the reduction and corrosion reactions leads to a significant increase of pH- values and causes the *E*h of the water passing through the barrier to decrease [*Bennett*, 1997; *Blowes et al.*, 2000]. It appears likely that high pH conditions promote the precipitation of a number of secondary minerals throughout the treatment zone. These reactions consume alkalinity and act to buffer further increases in pH [*Bennett*, 1997; *Blowes et al.*, 2000]. The exsolution of dissolved gases may act to buffer the redox potential of the pore water.

The ground water leaving the treatment zone is characterized by low dissolved species concentrations and exhibits high pH- and low *E*h-conditions [*Bennett*, 1997]. However, pH and *E*h are restored to near background values downgradient of the reactive barrier, indicating that reactions with the native aquifer material are buffering the infiltrating high pH, low *E*h water. This zone is termed “buffer zone,” since interactions with the native aquifer minerals will tend to re-establish a new equilibrium condition. Important processes for pH- buffering may be the dissolution of aluminosilicate and clay minerals and the sorption of silicic acid combined with the release of protons [*Powell et al.*, 1995]. The desorption of hydrogen ions from oxide and clay mineral surfaces may be an additional, possibly more important, pH- buffering process. The reductive dissolution of oxides and oxy-hydroxides and possibly degassing may be responsible for the observed *E*h-increase.

The conceptual model is applicable for the zones located upgradient and within any zero-valent iron reactive barrier. However, geochemical processes controlling pH- and *E*h-buffering downgradient of the reactive barrier depend on the site-specific mineralogy and, therefore, apply only to the Elizabeth City site.

Definition of Reaction Network

This section introduces the reaction stoichiometries, rate expressions and equilibrium constants of the reactions considered in this study based on the conceptual model by *Bennett* [1997]. In general, the equilibrium constants were taken from the database of MINTEQA2 [*Allison et al.*, 1991], unless otherwise noted. All reactions considered can be expressed in terms of the following 27 components: Al^{3+}, Ca^{2+}, Cl^{-}, $CH_4(aq)$, CO_3^{2-}, CrO_4^{2-}, $Cr(OH)_2^{+}$, DOC, Fe^{2+}, Fe^{3+}, H^{+}, $H_2(aq)$, H_4SiO_4, HS^{-}, K^{+}, Mg^{2+}, Mn^{2+}, Na^{+}, NH_4^{+}, NO_3^{-}, $O_2(aq)$, SO_4^{2-}, TCE, cis-1,2 DCE, VC, ethane and H_2O.

Complexation Reactions

Table 1 lists all 79 aqueous complexes considered in this study along with the corresponding equilibrium constants reported as dissociation constants.

Reduction-corrosion Reactions

The conceptual model considers the reduction of hexavalent chromium, of the chlorinated organic compounds, and of other oxidized species dissolved in the ambient ground water. Due to its extreme reduction capacity, zero-valent iron ultimately leads to the reduction of all electron acceptors [*Bennett*, 1997; *Blowes et al.*, 2000] including dissolved oxygen [*MacKenzie et al.*, 1997], Mn(IV), Fe(III), nitrate [*Rahman and Agrawal.*, 1997; *Cheng et al.*, 1997], sulfate, DIC, DOC [*Weathers et al.*, 1995, *Orth and Gillham*, 1996] and the solvent water itself [*Reardon*, 1995]. In the present study, it was assumed that dissolved manganese occurs exclusively as Mn(II); the reduction of Mn(IV) was, therefore, neglected. Furthermore, it was assumed that ferric iron can occur as a reaction product of iron corrosion, if the half reaction for the electron acceptor considered has a higher standard potential than the half reaction for the Fe^{2+}/Fe^{3+} redox couple. For example, *Powell et al.* [1995] reported that the corrosion of zero-valent iron in the presence of oxygen produces ferric iron. Ferric iron reduction was excluded in this study.

The reaction stoichiometries of all reduction-corrosion reactions were normalized with respect to zero-valent iron. The degradation of the organic compounds by reductive elimination and hydrogenolysis was considered. It was assumed that hydrogenolysis leads to the sequential degradation of TCE (C_2HCl_3) to cis-1,2 DCE ($C_2H_2Cl_2$), VC (C_2H_3Cl), and ethane (C_2H_6) [*Bennett*, 1997; *Blowes et al.*, 2000]. Laboratory experiments [*O'Hannesin et al.*, 1995] conducted using water from the Elizabeth City site and zero-valent iron indicated that only 7% of TCE was degraded by hydrogenolysis to cis-1,2 DCE. When determining the reaction stoichiometry of TCE-degradation, it was assumed that the remaining 93% is directly degraded to ethane.

All reduction-corrosion reactions are assumed to be irreversible. The reaction rate of hexavalent chromium reduction by zero-valent iron is characterized by a square root dependence on Cr(VI) and H^+ and is proportional to the reactive surface area of zero-valent iron [*Gould*, 1982]. For all other electron acceptors except water, it was assumed that the reaction rate is first order with respect to the electron acceptor and proportional to iron surface area. Iron corrosion by water was described by a rate expression with a first order dependence on iron surface area [*Reardon*, 1995]. Since this reaction is not dependent on the concentration of the electron acceptor, it was assumed that the reaction rate approaches zero, when equilibrium conditions are approached. An equilibrium constant of log $K_{Fe^0(s)_{H_2O}}$ = -11.78 was calculated based on data from *Reardon* [1995] and *Stumm and Morgan* [1996].

Secondary reactions between reduced reaction products (e.g., hydrogen gas, hydrogen sulfide, methane or ammonia) and oxidized species (e.g., hexavalent chromium, dissolved oxygen, nitrate and sulfate) may lead to inhibitive or competitive effects influencing the reaction progress of a particular reduction-corrosion reaction. For example, *Siantar et al.* [1995] observed that the presence of oxygen or nitrite affected the degradation of pesticide by zero-valent iron, indicating that inhibition or competition may play a role. Inhibitive or competitive effects are neglected here and reduction-corrosion reactions are assumed to occur as parallel reactions.

Table 2 summarizes the reaction stoichiometries of the reduction-corrosion reactions considered. The total iron corrosion rate can be estimated as the sum of all reduction-corrosion rates.

Formation of Secondary Minerals in Treatment Zone

The conceptual model also accounts for the precipitation of secondary minerals within the treatment system. The reaction stoichiometries of the reduction-corrosion reactions in Table 2 imply a net pH- increase creating conditions favorable for the precipitation of carbonate minerals and hydroxide mineral phases [*Bennett*, 1997; *Blowes et al.*, 2000]. In addition supersaturated conditions were observed locally with respect to iron sulfide minerals [*Bennett*, 1997; *Blowes et al.*, 2000].

Examination of the core samples by scanning electron microscopy (SEM) and transmission electron microscopy (TEM) identified the possible occurrence of amakinite ($Fe(OH)_2$), goethite (α-FeOOH) or akagenite (ß-FeOOH) [*Palmer,* 1999]. It was determined that $Fe(OH)_2$ is the mineral phase most likely present as a secondary precipitate [*Palmer,* 1999]. Secondary carbonate and sulfide mineral phases could not be identified; however, this may be due to the low volume fractions or the amorphous nature of these mineral phases.

The precipitation of secondary mineral phases A_i^m is described by rate expressions based on transition state theory [*Lasaga,* 1998]:

$$R_i^m = -k_{eff,i}\left(1 - \frac{IAP_i^m}{K_i^m}\right) \tag{22}$$

where $k_{eff,i}$ is an effective rate constant for the dissolution of the mineral phase A_i^m, IAP_i^m is the ion activity product and K_i^m defines the corresponding equilibrium constant. Reactions describing the formation of secondary mineral phases within the treatment zone are summarized in Table 3. The equilibrium constant for $Fe(OH)_2$(am) was taken from the database of EQ3/EQ6 [*Wolery et al.,* 1990].

pH- and E*h-buffering Downgradient of Barrier*

pH -buffering

The water exiting the reactive barrier is characterized by alkaline conditions with pH- values ranging from 9 to 11 [*Bennett*, 1997, *Blowes et al.*, 1999]. This strongly alkaline pore water is likely to interact with the native aquifer material downgradient of the barrier. According to *Puls et al.* [1992] and *Palmer* [1999], the mineralogy of the aquifer consists

primarily of aluminosilicate minerals. The primary minerals present in the aquifer sediments are quartz > albite > sanidine > muscovite and kaolinite [*Puls et al*., 1992]. *Powell et al*. [1995] reported that the aquifer material from the Elizabeth City site is capable of buffering the pH towards neutral conditions by the dissolution of aluminosilicate and clay minerals. An additional source of acidity may be the sorption of silicic acid, originating from Si-mineral dissolution, onto iron-oxide/hydroxide surfaces combined with the release of hydrogen ions [*Powell et al*., 1995].

In preliminary simulations, it was assumed that pH- buffering is due to the dissolution of kaolinite. The pH dependent rate expression given by *Carroll and Walther* [1990] was used. The field-observed pH- buffering could only be reproduced by disallowing the precipitation of gibbsite and $Al(OH)_3$(am) and by setting the reactive surface area for kaolinite to values of 10^7 m^2 mineral surface per m^3 bulk porous medium. The field data [*Bennett*, 1997; *Blowes et al*., 1999] is characterized by low dissolved Al-concentrations downgradient of the barrier indicating that aluminosilicate dissolution is not as pronounced or that gibbsite or $Al(OH)_3$(am) precipitation occurs. The effect of sorption of silicic acid and subsequent release of protons was not investigated here. However, a similar kaolinite reactive surface area would be necessary to reproduce the observed pH- buffering, because sorbing silica is originating from the dissolution of the aluminosilicates. Sequential extraction tests conducted by *Palmer* [1999] revealed that much of the extractable Al immediately downgradient of the reactive barrier is present in amorphous form. This is not the case for the undisturbed aquifer material upgradient of the barrier, where most of the extractable Al is crystalline. This indicates that weathering of Al-Si mineral phases with the subsequent precipitation of an amorphous Al-bearing phase, possibly $Al(OH)_3$(am), is taking place.

It is likely that other processes also contribute to pH- buffering. Another possible explanation for the observed pH-buffering is the desorption of hydrogen ions from oxide and clay mineral surfaces, which have been in contact with the slightly acidic ambient ground water prior to installation of the reactive barrier. The desorption of hydrogen ions can be described as [*Stumm and Morgan,* 1996]:

$$S - OH_2^+ + OH^- \leftrightarrow S - OH + H_2O \tag{23}$$

$$S - OH + OH^- \leftrightarrow S - O^- + H_2O \tag{24}$$

A surface complexation model can be used to describe this pH- buffering process. However, such a model is presently not included in MIN3P. This process is, therefore, approximated as a release of hydrogen ions from a limited reservoir, until the pH reaches circumneutral values. It should be noted that *Palmer* [1999] determined from extraction tests significantly higher concentrations of exchangeable cations downgradient of the barrier than upgradient of the barrier (≈ 1 meq/100 g soil). This may be caused by the desorption of H^+-ions followed by the sorption of cations from solution.

Eh-buffering

The treated pore water exiting from the reactive barrier is extremely reducing due to the presence of reduced gaseous species such as dissolved hydrogen gas, H_2S(aq), ammonia and methane. *Bennett* [1997] and *Blowes et al.,* [2000] observed *E*h-values locally lower than -500 mV. Reduced gaseous species may either degas or react with Mn- and Fe-oxides and oxy-hydroxides contained in the aquifer material. Iron oxy-hydroxides are abundant in the native aquifer mineral, while manganese oxides occur at lower concentrations [*Puls*, personal communication, 1998; *Palmer*, 1999]. Degassing was observed at the Elizabeth City site within the reactive barrier, but may not be an important process downgradient of the treatment system. *Appelo and Postma* [1993] and *Stumm and Morgan* [1996] give redox half reactions for the oxidation of the relevant dissolved gas species and the reduction of Mn- and Fe-mineral phases, which can be combined to describe *E*h-buffering reactions possibly occurring downgradient of a reactive barrier. The field data [*Bennett,* 1997; *Blowes et al*., 2000] does not indicate the oxidation of H_2S(aq) and methane, since sulfate concentrations at the monitoring well located 1 m downgradient of the barrier are negligible, and methane concentrations remain high. Data for ammonia was not available. These data indicate that these reactions are not taking place. *E*h-buffering reactions involving the consumption of H_2S(aq), ammonia and methane are, therefore, neglected. However, Fe-and Mn-oxides may undergo reductive dissolution when in contact with dissolved hydrogen gas emanating from the barrier. Assuming that iron and manganese oxides can be represented by goethite and pyrolusite, overall reactions for the oxidation of dissolved hydrogen gas combined with the reductive dissolution of the mineral phases can be written as:

$$FeOOH(s) + 2H^+ + \tfrac{1}{2} H_2(aq) \rightarrow Fe^{2+} + 2H_2O \tag{25}$$

$$MnO_2(s) + 2H^+ + H_2(aq) \rightarrow Mn^{2+} + 2H_2O \tag{26}$$

The equilibrium constant for the reductive dissolution of pyrolusite combined with the oxidation of H_2(aq) (log K = -43.9640) was calculated based on redox half reactions as reported by *Stumm and Morgan* [1996]. The appropriate equilibrium constant for goethite (log K = -13.5940) was obtained from equilibrium constants in the MINTEQA2-database

[*Allison et al*., 1991] and from *Stumm and Morgan* [1996]. These reactions are described by a transition state theory rate expression of the form [*Lasaga*, 1998]:

$$R_i^m = -S_i k_i \left(1 - \frac{IAP_i^m}{K_i^m} \right) \tag{27}$$

which includes reactive surface area and allows the update of mineral reactivity with progressing dissolution.

The reductive dissolution of iron and manganese oxides according to equations 25 and 26 consumes acidity. This additional pH- increase may enhance the depletion of the pH- buffer capacity of the aquifer. The reductive dissolution of oxides and oxy-hydroxides will also lead to an increase in dissolved ferrous iron and manganese concentrations. It is possible that these concentration increases will be controlled by the precipitation of siderite and rhodochrosite, respectively. Hydroxides such as $Fe(OH)_2$(am) and amorphous pyrocroite ($Mn(OH)_2$(am)) precipitate only in alkaline waters, and are, therefore, incapable of controlling dissolved iron and manganese concentrations downgradient of the barrier.

Solution Domain and Model Parameters

One-dimensional and two-dimensional reactive transport analyses were conducted. The two-dimensional solution domain is a vertical cross section through the center of the reactive barrier, as illustrated in Figure 4, and is aligned along Transect 2 (Figure 2). The solution domain extends 4 m in the horizontal direction and 3.2 m in the vertical direction and ground-water flow takes place from the left to the right. The domain contains the multi-level monitoring wells 21-25, which have been installed upgradient, within and downgradient of the reactive barrier (Figure 2, Figure 4), [*Bennett*, 1997; *Blowes et al*., 1999]. Each well contains 7 monitoring points providing a detailed description of the geochemical composition of the ground water entering the solution domain. The approximate location of the 0.6 m thick reactive barrier is indicated by the dashed vertical lines. One-dimensional simulations were carried out along the flowline carrying the highest chromium concentrations towards the barrier. The field data indicates that this flowline follows a zone of preferential flow and passes through monitoring points 21-5, 22-3, 23-3, 24-3 and 25-5 [*Bennett*, 1997; *Blowes et al*., 2000], as indicated in Figure 4.

Spatial Discretization

The discretized solution domain for the two-dimensional simulation is shown in Figure 5. A discretization interval of 10 cm in both vertical and horizontal directions was used. The discretization was refined to 5 cm in the horizontal direction within and in the direct vicinity of the reactive barrier to facilitate a more accurate representation of rapid geochemical changes within and downgradient of the treatment system. This discretization leads to 50 grid points in the horizontal direction and 33 grid points in the vertical direction (Figure 5). For the one-dimensional simulations, a discretization interval of 2.5 cm was used within and in the vicinity of the treatment zone leading to a total number of 68 grid points.

Physical Parameters and Hydraulic Conductivity Distribution

Field measurements indicated a hydraulic gradient varying between 0.0011 and 0.0033 during the sampling intervals [*Bennett*, 1997; *Blowes et al*., 1999]. For the modeling study it was assumed that a hydraulic gradient of 0.0022 can be used to represent average flow conditions. The hydraulic head loss along the vertical cross section is negligible and recharge is insignificant, because the ground surface is paved above the treatment system [*Bennett*, 1997]. The flow system is modeled as a fully saturated system with no flow boundaries at the top and the bottom of the domain and first type boundaries at the upgradient and downgradient boundaries. The upper portion of the aquifer was found to be less hydraulically conductive than the underlying layers [*Bennett*, 1997; *Blowes et al*., 2000]. The field observations of *Puls et al.* [1995] and *Bennett* [1997] indicate the presence of a highly conductive layer, which is located roughly 4.5 - 6.5 m below ground surface. Significant hydraulic conductivity variations lead to large differences in ground-water flow velocities with depth [*Bennett*, 1997]. Constant head and rising head response tests showed hydraulic conductivity values ranging from 1.2×10^{-5} to 1.9×10^{-4} m s^{-1} within the aquifer and ranged from to 1.2×10^{-7} to 2.3×10^{-3} m s^{-1} within and in the vicinity of the reactive barrier [*Bennett*, 1997; *Blowes et al*., 2000]. Hydraulic conductivities have been assigned to the two-dimensional solution domain based on the hydraulic response and the modeling analysis conducted by *Bennett* [1997] (Figure 6 and Table 4). Locally isotropic conditions were assumed in this context.

For the one-dimensional simulations the hydraulic conductivity in the aquifer was estimated to be $K = 8.1 \times 10^{-5}$ m s^{-1}, while a hydraulic conductivity of $K = 1.2 \times 10^{-3}$ m s^{-1} was assigned to the treatment zone. High hydraulic conductivities in the reactive barrier can be explained by a relatively loose packing of the treatment material as a result of the installation procedure [*Bennett,* 1997]. *Bennett* [1997] estimated a porosity within the reactive barrier of approximately 0.43-0.62. It

was assumed that the porosity of the barrier is $\phi = 0.5$ within the high hydraulic conductivity zones. A porosity of $\phi = 0.38$ was assumed to be representative for the aquifer and the low hydraulic conductivity zones in the barrier. Dispersive and diffusive transport processes were neglected, since the problem can be characterized as advection-reaction dominated. This simplification eliminates adverse effects of artificial dispersion at the upgradient side of the reactive barrier on the simulation results.

Mineralogical Parameters

The volume fraction for zero-valent iron is $\varphi_{Fe_0(s)} = 0.5$ and $\varphi_{Fe_0(s)} = 0.62$ for porosities of $\phi = 0.5$ and $\phi = 0.38$, respectively. Only qualitative information is available regarding the volume fractions of the minerals contained in the aquifer [*Puls et al.*, 1992]. The bulk of the aquifer material was assumed to be non-reactive. The dissolution of kaolinite and other aluminosilicate minerals was excluded, because the preliminary simulations showed that these reactions are not likely to be important for controlling pH and the geochemical composition of the pore water. The dissolution reactions considered include pyrolusite and goethite, which are important for *E*h-buffer reactions downgradient of the reactive barrier. The volume fractions of these minerals have been estimated to allow at least a generic description of the specified buffer reactions. The estimated mineral volume fractions are summarized in Table 5. Mineralogical analyses of the aquifer material [*Palmer*, 1999] indicate that the goethite content was estimated correctly (measured: 5.5×10^{-4} - 1.4×10^{-3} m^3 mineral m^{-3} bulk), while the MnO_2-content was overestimated (measured: 2.2 - 6.5×10^{-6} m^3 mineral m^{-3} bulk). When conducting the simulations, there was no information available regarding the degree of surface protonation in the sediment prior to installation of the reactive barrier. It was assumed that 50 mol H^+ per m^3 bulk porous medium are available for desorption when in contact with the infiltrating high pH waters.

The largest uncertainty with respect to determining reaction rates can be attributed to reactive surface area estimates. Reactive surface areas for the treatment material used at the field site are presented in Table 6 based on data reported by *Bennett* [1997]. It is apparent that the specific reactive surface area is more than 500 times larger than the geometric surface area calculated based on the average grain size d_{50}. Differences between geometric and reactive surface areas may be explained by the large intragranular porosity of zero-valent iron. The density of the treatment material can be calculated based on the bulk density from laboratory studies and is $\gamma = 4.77$ g cm^{-3}, which is much lower than average literature values for native iron ($\gamma = 7.3$-7.9 g cm^{-3}, [*Klein and Hurlbut*, 1993]. This deviation indicates that the treatment material is characterized by a pronounced secondary porosity.

The reactive surface areas of goethite and pyrolusite were estimated, since no site-specific information was available and are summarized in Table 7. All other minerals considered in this study are secondary minerals and effective rate constants were used, which implicitly include reactive surface areas. The reactive surface areas of zero-valent iron, goethite and pyrolusite are updated, as the minerals become depleted.

Boundary and Initial Chemical Composition of Ground Water

Geochemical data from *Bennett* [1997] was used to define the boundary and initial condition in the solution domain. The chemical composition of water samples from monitoring well 21, which is located upgradient of the reactive barrier (see Figures 2 and 4), was analyzed on temporal variability. It was found that the general geochemical composition of the ground water remained constant over time. The data from November 1996 was used to describe the source concentrations upgradient of the treatment system.

pH and *E*h were taken from field measurements. The *E*h was slightly increased for the sampling points 21-3, 21-5 and 21-7 to allow the determination of ammonia from nitrate based on the assumption of equilibrium for the NO_3^-/NH_4^+ redox couple. Total dissolved carbonate concentrations were obtained from field measured alkalinity [*Bennett*, 1997] using MINTEQA2 [*Allison et al.*, 1991]. Field measured total concentrations were used for Ca^{2+}, Cl^-, K^+, H_4SiO_4, Mg^{2+}, Mn^{2+}, Na^+, NO_3^-, O_2(aq) and SO_4^{2-} [*Bennett*, 1997]. The data for dissolved oxygen was not available for November 1996 and data from June 1997 was used instead. Field measured concentrations from *Bennett* [1997] were also used for the chlorinated organic compounds TCE, cis-1,2 DCE, VC, ethane and methane. The field data for total dissolved organic carbon, expressed in terms of CH_2O [*Bennett*, 1997] was corrected for the chlorinated organic compounds, which are considered separately. Dissolved hydrogen gas concentrations were calculated based on pH and *E*h. *Puls et al.* [1992] reported that more than 98% of dissolved chromium is present as Cr(VI) in the contaminated ground water, since the reduction capacity of the aquifer material with respect to hexavalent chromium is low. It, therefore, was assumed that total dissolved chromium can be used to represent hexavalent chromium. This assumption is consistent with field-measured hexavalent chromium concentrations, which coincide well with analytically determined total chromium concentrations [*Bennett*, 1997]. Trivalent chromium concentrations were determined based on the assumption of equilibrium with amorphous chromium hydroxide. Total ferrous and ferric iron concentrations were close to or below detection in the upgradient portion of the aquifer and were determined based on the assumption of equilibrium with goethite and equilibrium conditions for the Fe^{2+}/Fe^{3+} redox couple. Total NH_4^+ and HS^- concentrations were not analyzed for and were

calculated assuming equilibrium for the NO_3^-/NH_4^+ and SO_4^{2-}/HS^- redox couples, respectively. Dissolved aluminum concentrations were determined by equilibrating the ground water with kaolinite.

The initial condition in the solution domain affects the simulation results only at early time. The chemical composition of the water samples taken from monitoring point 21-7 was, therefore, used to describe the initial condition in the entire aquifer.

Calibrated Rate Constants

Some of the reaction rates used in this study were determined in laboratory experiments using ground water from the field site [*O'Hannesin et al*., 1995; *Bennett*, 1997; *Blowes et al*. 2000]. The rate constants, therefore, include influences due to the interactions with other dissolved species and can be applied directly in the modeling study, provided that laboratory conditions are representative for conditions encountered in the field. In other cases, laboratory-derived rate constants are based on ideal, single component experiments. It may not be possible to use these rate constants, since they do not account for complex interactions between reduced and oxidized species. Instead, a calibration procedure has to be used to determine effective reaction rates. The calibration of these rate constants was conducted with the objective to reproduce concentrations of dissolved reactant and product species similar to those observed in the field. This approach is justified, because zero-valent iron acts as the ultimate electron donor in the system. However, the application of the method is limited, because calibrated rate constants represent apparent rate constants and may vary significantly depending on the specific geochemical composition of the ground water in contact with zero-valent iron. These variations were neglected in the present study.

Preliminary simulations were conducted to approximately calibrate the model with respect to aqueous concentrations observed in the field [*Bennett*, 1997; *Blowes et al*., 2000]. The calibration was carried out for the one-dimensional solution domain. Effects due to preferential flow or varying water chemistry were, therefore, not taken into account. The calibrated rate constants were used for the one- and two- dimensional simulations presented here.

The simulated data was compared to field observations from February 1997 (240 days after completion of the barrier installation). The calibration involved adjusting the rate constants for reduction-corrosion reactions, the reactive surface area of zero-valent iron, and effective rate constants for the precipitation of secondary minerals. Table 10 shows a list of the components and source and sink terms affecting the component concentrations. This table identifies the interactions between the components and the effect of dissolution-precipitation reactions and serves as a basis for the calibration procedure.

It was assumed that the laboratory-derived rate constants for reductive dechlorination of TCE, cis-1,2 DCE and vinyl chloride [*O'Hannesin et al*, 1995; *Bennett*, 1997] are representative for the conditions at the site. These rate constants appear to be most reliable, since the experiments were conducted with the treatment material used at the field site and with the Elizabeth City ground water. To approximately match the field data, it was necessary to decrease the reactive surface area for zero-valent iron listed in Table 6 by one order of magnitude. This difference may be attributed to scaling from laboratory to field conditions. Possible reasons for this scaling include locally higher flow velocities in the field or mixing of the treatment material with the native aquifer material during installation. The reactive surface area used in the simulations was 3.88×10^5 [m^2 mineral m^{-3} mineral]. The rate constant for hexavalent chromium reduction was taken directly from the laboratory study by *Gould* [1982]. The remaining rate constants were obtained by calibration in an attempt to match the concentrations of the various electron acceptors and reaction products (Table 11). The table also includes laboratory-derived rate constants for nitrate reduction and iron corrosion by water for comparative purposes. Discrepancies between the calibrated and measured reaction rates will be addressed in a later section along with the discussion of the simulation results.

Effective rate constants for the precipitation of secondary mineral phases were adjusted to approximately reproduce dissolved Cr^{3+}, Ca^{2+}, Mg^{2+}, Mn^{2+}, Fe^{2+}, Fe^{3+}, HS^- and CO_3^{2-} concentrations and pH. The resulting rate constants are listed in Table 12. Rate constants for the reductive dissolution of goethite and pyrocroite were estimated. Since these minerals are relatively insoluble, comparable slow reaction kinetics have been assumed. The rate constants are summarized in Table 13.

Results and Discussion

In the following sections, the results of the one- and two-dimensional simulations are presented and discussed. The simulations represent quasi-steady state conditions with respect to the dissolved contaminant concentrations. Quasi-steady state conditions prevail because the volume fraction of the treatment material is large in comparison with the contaminant and other electron acceptor concentrations entering the treatment system.

One-dimensional Simulations

The simulations presented here are based on a simplified one-dimensional flow field. The effect of the complex flow conditions characteristic for the site cannot be reproduced using this approach. On the other hand, two-dimensional simulations enhance the complexity and make an interpretation of the geochemical data more difficult. The results of the one-dimensional simulations conducted here are compared directly to field observations from February 1997, corresponding to 240 days of barrier operation [*Bennett*, 1997; *Blowes et al.*, 2000].

Removal of Contaminants

Figure 7a illustrates the removal of hexavalent chromium by the treatment system. The simulations show very rapid reduction of hexavalent chromium. The results are not sensitive to the chromium reduction rate, since the time scale of chromium removal is much shorter than the time scale of advective transport through the barrier. Trivalent chromium concentrations never increase significantly, since the conditions in the barrier favor the precipitation of amorphous chromium hydroxide [*Bennett*, 1997; *Blowes et al.*, 2000]. The combination of the reduction and precipitation reactions leads to low hexavalent and trivalent chromium concentrations within and downgradient of the reactive barrier, and are in agreement with field measured total chromium concentrations, which are below the detection limit of 0.01 mg L^{-1} [*Bennett*, 1997; *Blowes et al.*, 2000].

The simulated and measured concentrations of the chlorinated organic compounds and ethane are depicted in Figure 7b. The model results show that concentrations of TCE, cis-1,2 DCE and VC decline by 1-3 orders of magnitude across the barrier, while ethane concentrations increase to values above the detection limit. These results are generally in agreement with the field observations by *Bennett* [1997]. Within the barrier system, TCE is partly reduced to ethane and cis-1,2 DCE. The simulated vinyl chloride concentrations increase temporarily due to the degradation of cis-1,2 DCE. As indicated by the rate constants shown in Table 11, the reduction of the chlorinated organic compounds is not as rapid as the reduction of chromium and the transformation remains incomplete. Primarily affected are the degradation products cis-1,2-DCE and VC. The results agree reasonably well with the field data [*Bennett*, 1997; *Blowes et al.*, 2000]. TCE-concentrations downgradient of the barrier are below detection limit of 1 µg/l, while cis-1,2-DCE and VC persist in low, but measurable concentrations. The simulation significantly overpredicts ethane concentrations, suggesting that ethane is not the degradation product, or that ethane is further degraded, possibly to inorganic carbon.

Reduction of Electron Acceptors

Figure 8 compares the computed concentrations for nitrate and sulfate to the field-measured concentrations. The trend of the model results is in agreement with the field data. The concentration of the reaction products sulfide and ammonia are also shown. Nitrate reduction is rapid and field measured concentrations fall below the detection limit in the entry portion of the barrier [*Bennett*, 1997]. Field measured ammonia concentrations are not available; a mass balance between nitrate and ammonia is, therefore, not possible. Sulfate concentrations decrease also by 1-2 orders of magnitude. The reaction product hydrogen sulfide does not reach significant concentrations indicating that the precipitation of mackinawite is taking place (see below), even though sulfide mineral phases could not be identified in mineralogical analyses [*Palmer*, 1999].

Selected Cation Concentrations

Figure 9 compares computed concentrations for selected cations to analytical concentrations from *Bennett* [1997]. The simulated results are consistent with the field observations, which show declining dissolved cation concentrations while the pore water is flowing through the barrier. The decrease of cation concentrations indicates that secondary minerals precipitate in the treatment system, as was discussed by *Bennett* [1997] and *Blowes et al.* [2000]. The simulated results for calcium and magnesium compare well with the field data, except for the buffer zone downgradient of the barrier, where magnesium concentrations are overpredicted. The lower field-measured concentrations may be due to surface complexation reactions, involving the desorption of protons as a result of the infiltrating high pH water in conjunction with the sorption of Mg. This hypothesis is supported by the elevated exchangeable Mg-concentrations observed downgradient of the barrier [*Palmer*, 1999]. The solubility of manganese was assumed to be controlled by rhodochrosite. However, the model results overpredict dissolved manganese concentrations in the treatment zone and downgradient of the barrier. This indicates that Mn does not precipitate as rhodochrosite, but may co-precipitate with other carbonate minerals. The pore water also becomes slightly supersaturated with respect to amorphous pyrocroite [$Mn(OH)_2$(am), SI_{max} = 0.5], which may be an additional sink for dissolved manganese. Dissolved Mn-concentrations may also be limited by sorption or ion-exchange reactions [*Palmer*, 1999]. The model results overpredicted dissolved iron concentrations slightly and underpredicted carbonate concentrations (not shown). It is possible that Mg does not precipitate as a carbonate mineral phase, but rather as brucite [$Mg(OH)_2$, SI_{max} = 1.2]. The pore water also reached supersaturated conditions with respect to artinite [$Mg_2CO_3(OH)_2$, SI_{max} = 0.2]. If this is the case, dissolved carbonate becomes less depleted, while the

precipitation of siderite may be more extensive. On the other hand, the precipitation of Ca-hydroxides, such as portlandite ($Ca(OH)_2$), is unlikely (SI_{max} = -5.2), since the pH in the pore water is not sufficiently alkaline.

*pH and E*h

Reduction-corrosion reactions taking place in the treatment zone lead to a pronounced pH- increase and a decrease of the redox-potential of the ground water passing through the barrier [*Bennett*, 1997]. Figure 10 shows the results for pH and *E*h for the one-dimensional simulation. The pH of the ground water upgradient of the reactive barrier is approximately 6.3 and rises in the wall to values up to 9-11. Within the treatment zone, the simulation results agree very well with field-measured pH- values. The field data from *Bennett* [1997] show that pH- values downgradient of the barrier drop rapidly and approach close-to-background values. It was assumed that pH- buffering is due to deprotonation from mineral surfaces. The observed strong pH- buffering could only be reproduced by specifying a large reservoir of sorbed hydrogen ions (50 mol m^{-3} porous medium). Assuming that the observed increase in exchangeable cations downgradient of the reactive barrier [*Palmer*, 1999] is due to desorption of H^+ followed by sorption of dissolved cations, the amount of hydrogen ions desorbed can be calculated as approximately 17 mol per m^3 bulk porous medium (ϕ = 0.38, ρ_b = 1643 kg m^{-3}). This value agrees relatively well with the estimated H^+ available for desorption and further supports that deprotonation indeed may be an important pH- buffer process downgradient of the barrier.

It is likely that, if hydrogen gas is present in sufficient quantities, *E*h measurements reflect the state of the $H_2(aq)/H^+$ redox couple. Therefore, the redox potential was computed based on dissolved hydrogen gas concentrations. The pore water entering the barrier is characterized by *E*h-values of approximately 400-500 mV. The simulation results show a rapid decrease of *E*h within the reactive barrier to values below -500 mV. Although the field-measurements used for this comparison are less reducing than calculated by the model, E_h-values lower than -550 mV have been measured locally in the treatment zone at other locations and sampling times [*Bennett*, 1997; *Blowes et al.*, 1999]. *E*h-values increase up to close to background-values of 200 - 400 mV downgradient of the reactive barrier [*Bennett*, 1997] due to *E*h-buffer reactions. The reductive dissolution of goethite and pyrolusite overpredicts *E*h-buffering in the downgradient zone indicating that these reactions are characterized by slow reaction kinetics. Unlike pH- buffering, *E*h-buffer reactions do not require a large reservoir of buffer agents. This is due to the comparably low $H_2(aq)$-concentrations leaving the treatment zone and the apparent persistence of other reduced dissolved gases, such as methane and $H_2S(aq)$ (not shown).

Discussion of Reaction Mechanisms

In order to approximately match the field data, the rate constant for nitrate reduction had to be increased by one order of magnitude, while the iron corrosion rate by water had to be decreased by four orders of magnitude in comparison to laboratory-derived rate constants (Table 11). Large uncertainties exist with respect to the applicability of the rate constant for nitrate reduction [*Rahman and Agrawal*, 1997] to the reactive barrier at the Elizabeth City site, since the tested treatment material was different, and the reported rate constant had to be corrected for reactive surface area. The discrepancies with respect to the rate constant for nitrate reduction were, therefore, considered within the uncertainty of the rate constant derived from the work of *Rahman and Agrawal* [1997].

The differences between the measured rate constant for iron corrosion by water [*Reardon,* 1995] and the corresponding calibrated rate constant is more significant (Table 11). Modeled *E*h-values (based on the $H_2(aq)/H^+$ redox couple) still fall notably below the field measured values, despite the decreased rate constant for iron corrosion by water. The laboratory-derived reaction rate from *Reardon* [1995] (0.7 mmol kg^{-1} Fe day^{-1}) was normalized with respect to reactive surface area. In this context, it was assumed that the reactive surface area reported by *Reardon* [1995] is representative for the investigated material, which was put into question in the original reference. The differences may be explained by the significant rate of sulfate reduction at the field site in Elizabeth City (Figure 8). Sulfate reduction at the Elizabeth City site may be microbially mediated, as proposed by *Bennett* [1997]. In this case, dissolved hydrogen gas may be used as the electron donor. In the present modeling study, sulfate reduction was described as a heterogeneous reaction between sulfate and zero-valent iron. However, the following reaction sequence may better describe the reaction mechanisms controlling the geochemical conditions at the field-site:

$$4Fe^0(s) + 8H_2O \rightarrow 4Fe^{2+} + 8OH^- + 4H_2(aq) \quad (28)$$

$$SO_4^{2-} + 4H_2(aq) \rightarrow HS^- + OH^- + 3H_2O \quad (29)$$

$$4Fe^{2+} + HS^- + 7OH^- \rightarrow FeS(am) + 3Fe(OH)_2(am) + H_2O \quad (30)$$

This reaction sequence leads to a net pH- increase, the removal of sulfate and dissolved hydrogen gas, and the immobilization of the reaction products iron and sulfide. Nevertheless, it is also possible that sulfate is simultaneously reduced by the direct interaction with zero-valent iron (Table 2). Hydrogen gas may also be consumed as an electron

donor in other reduction reactions (nitrate, DIC and DOC, *Lovley and Goodwin*, 1988). These reactions may explain the apparent iron corrosion rates by water. Microbially-mediated reduction reactions in porous media composed of zero-valent iron and involving hydrogen gas as the electron donor were previously reported by *Weathers et al.* [1995]. It is not possible to uniquely describe the contributions of the various reaction processes.

Corrosion of Zero-valent Iron

The simulation results indicate that iron corrosion is most significant in the entry area of the barrier and decreases along the flow path, when the electron acceptors become depleted. The reaction rates of selected reduction-corrosion reactions are shown in Figure 11. Nitrate and sulfate are the most important electron acceptors in the system, which is in agreement with the interpretation of *Bennett* [1997]. The reduction of hexavalent chromium also contributes to iron corrosion. The remaining electron acceptors are lumped together, since their contributions are comparably small. Figure 11 shows that chromium reduction only takes place in the entry area of the reactive barrier, since the reaction rate is fast in comparison to ground water velocities. The reduction of nitrate to ammonia is slower, and persists deeper into the barrier. The reduction of sulfate is characterized by even slower reaction kinetics. Reduction rates decrease continuously throughout the barrier, but are still discernable before leaving the treatment system into the downgradient portion of the aquifer. Figure 11 illustrates that the major contribution to iron corrosion is ultimately due to the reduction of sulfate. Iron corrosion due to the reduction of the chlorinated organic compounds is not explicitly presented in Figure 11, since the corrosion rates are negligible on the scale of the graph.

Precipitation of Secondary Minerals

Figure 12 shows that the precipitation of carbonate minerals, such as calcite and siderite, takes place close to the upgradient end of the barrier. Siderite is the dominant carbonate phase, because the corrosion of zero-valent iron liberates large amounts of ferrous iron. Small amounts of rhodocrosite also precipitate in the entry area of the barrier (not shown). It was assumed that the precipitation of a Ca-Mg-carbonate mineral phase controls aqueous Mg-concentrations. The formation of this mineral phase takes place throughout the barrier due to slow reaction kinetics. The real system will likely be characterized by the precipitation of a complex carbonate solid solution containing ferrous iron, calcium, magnesium and manganese rather than by the formation of distinct mineral phases [*Reardon*, 1995]. Ferric iron produced from iron corrosion also precipitates rapidly in the entry zone. On the other hand, minerals such as mackinawite and ferrous hydroxide precipitate throughout the treatment system. The formation of these mineral phases is controlled by the availability of the reactants, which are produced by sulfate reduction and iron corrosion by water. These results are consistent with the conceptual model of *Bennett* [1997]. Mineralogical analyses support the formation of secondary $Fe(OH)_2$ and possibly α-FeOOH [*Palmer*, 1999]. Carbonate and sulfide mineral phases were not found by *Palmer* [1999]. This may be due to the small volume fractions of these secondary precipitates (core samples were taken only two years after barrier installation), or due to the amorphous nature of these phases. However, mass balance considerations based on field-measured aqueous concentrations [*Bennett*, 1997; *Blowes et al.,* 2000] suggest that these mineral phases do form.

Long Term Efficiency

The tendency to locally precipitate relatively large amounts of secondary minerals over extended time periods may have an impact on the long term efficiency of a reactive barrier [*MacKenzie et al.*, 1997; *Bennett*, 1997]. Significant amounts of the treatment material may also be consumed due to the combined effect of sulfate reduction and iron-corrosion by water. Treatment material depletion in conjunction with secondary mineral formation may also affect the porosity of the treatment zone [*MacKenzie et al.*, 1997; *Bennett*, 1997].

Within the reactive barrier, the bulk porous medium consists at any time of porosity (void space), the volume fraction of the treatment material and the sum of the volume fractions of all secondary mineral phases. Figure 13 illustrates the potential for depletion of the treatment material and the precipitation of secondary minerals along the barrier after 5, 10 and 20 years of operation. Secondary minerals are not present initially and the porosity is $\phi = 0.5$ which is equal to the volume fraction of zero-valent iron. After 20 years the volume fraction of zero-valent iron has decreased from 0.5 to approximately 0.42 in the entry zone of the treatment system. However, the zone of significant treatment material depletion is limited to the first 10 cm of the barrier. At the same time, it can be observed that the porosity decreased over the 20 year simulation period from $\phi = 0.5$ to approximately $\phi = 0.36$ in the entry area of the barrier, indicating that a significant amount of secondary minerals has precipitated. The total volume fraction of secondary minerals can be estimated from the decrease of porosity and the depletion of the treatment material and amounts to a maximum value of $\phi = 0.22$ in the entry area of the reactive barrier. These results are comparable with porosity loss calculations performed by *Bennett* [1997] and *Blowes et al.* [2000].

The model results indicate that over a long period of time porosity may decrease significantly, which will almost certainly affect the hydraulic properties of the treatment system. More importantly, the reactivity of the treatment material may decline over time. In addition to the consumption of Fe^0, the accumulation of secondary mineral phases may compromise the reactivity of the remaining treatment material. It can be hypothesized that the reduction of the reactivity of the treatment material in the entry zone due to the precipitation of secondary minerals will allow the contaminants and other electron acceptors to pass this less reactive zone more or less unaffected. Reduction reactions will still occur in areas located deeper into the barrier, that have been less affected by the precipitation of secondary minerals. However, this process will decrease the effective thickness of the barrier and, therefore, the contact time of the contaminants with the treatment material. This may lead to the incomplete treatment of contaminants that require a long residence time. Although the potential for mass loss and secondary mineral formation has been identified previously [e.g., *MacKenzie et al.*, 1997; *Bennett*, 1997], the simulation results illustrate the distribution of iron-consumption and secondary mineral precipitation in a semi-quantitative way. In a real system, it can be expected that the depletion of the treatment material and the precipitation of secondary minerals is less concentrated in the inflow area than predicted in Figure 13, because decreasing iron reactivity was not accounted for in this study.

Two-dimensional Simulations

Two-dimensional simulations were carried out with input concentrations defined in Tables 8 and 9. The remaining geochemical parameters were as used in the one-dimensional simlations. These simulations illustrate the effect of preferential flow on the treatment of the contaminants. All results of the following reactive transport simulation represent conditions after 2 years of barrier operation.

Ground-water Flow

Figure 14 shows the streamlines constructed from the steady-state velocity field through the two-dimensional solution domain, which was calculated based on the hydraulic conductivity distribution presented in Figure 6 and is based on earlier work from *Bennett* [1997]. The model results indicate a heterogeneous flow field in the aquifer and through the reactive barrier. A zone of preferential flow exists in the reactive barrier at a depth of approximately 6 m below ground surface, which is consistent with the findings *of Puls et al.* [1995] and *Bennett* [1997].

Removal of Contaminants

The two-dimensional simulation clarifies the effect of the heterogeneous ground-water flow field on the treatment of contaminants. Figure 15 illustrates that the remediation of hexavalent chromium appears to be unaffected by the zones of preferential flow within the aquifer and the reactive barrier. The rapid reduction of hexavalent chromium ensures a successful treatment, even in zones of high flow velocities. Amorphous chromium hydroxide precipitates in a narrow fringe in the entry area of the treatment system.

Figure 16 shows the concentration distributions of the chlorinated organic compounds for the two-dimensional simulation. The concentration distribution upgradient of the reactive barrier does not coincide well with the concentration distribution of most inorganic compounds (e.g., chromium). This deviation may be due to the infiltration of TCE as a free phase product and subsequent dissolution in the source area [*Bennett*, 1997]. The simulation results indicate that zones of preferential flow may have a significant impact on the treatment of the organic compounds. The removal of the organics in areas of lower hydraulic conductivity are more pronounced, because of the longer contact time. cis-1,2 DCE and VC are treated to below MCL values (2µg/l VC and 7 µg/l cis1,2 DCE) in the upper portion of the solution domain, while the reductive dechlorination of TCE (MCL 5µg/l) in the lower portion of the domain leads to the production of these degradation products, which are only partially removed. The simulation results for chromium and the chlorinated organics agree reasonably well with field measured concentrations [not shown, see *Bennett*, 1997 or *Blowes et al.*, 2000].

*pH and E*h

Figure 17 presents the results for pH and *E*h. The effect of the heterogeneous flow field on these parameters can be clearly observed. pH- values increase more slowly within the reactive barrier in the zone of preferential flow. The pH-distribution is also affected by chemical heterogeneities. The concentrations of the electron acceptors entering the reactive barrier vary with depth, and higher pH- values can be correlated to high infiltrating electron acceptor concentrations. For example, sulfate concentrations are low in the upper and lower portion of the solution domain (Figure 18), resulting in a less pronounced pH- increase. This behavior may be an artifact of the decreased rate constants for iron corrosion by water, which were calibrated for conditions where sulfate is present, and may not be valid for conditions where sulfate is depleted. Elevated pH- values downgradient of the barrier can be observed in areas of high flow velocities, where the pH- buffer capacity of the aquifer is exhausted.

The redox potential decreases rapidly within the reactive barrier. The specified reaction network does not allow a consistent description of E_h-values, since hydrogen gas concentrations are assumed to be independent of the concentrations of electron acceptors such as nitrate and sulfate, which may be reduced with dissolved hydrogen gas as the electron donor. In areas where these electron acceptors are abundant, dissolved hydrogen gas concentrations may be lower than predicted by the simulations, while conditions may be more reducing in zones where the electron acceptors have been depleted. The E_h-increases downgradient of the barrier due to reductive dissolution of goethite and pyrolusite to close-to-background values.

Sulfate Reduction

Figure 18 illustrates the reduction of sulfate by the treatment system. Sulfate enters the reactive barrier primarily through the area of preferential flow, where it is reduced to dissolved hydrogen sulfide. However, hydrogen sulfide concentrations remain low, because mackinawite controls the solubility of HS^-. Low concentrations of HS^- are observed in selected zones located downgradient of the barrier. The model results indicate that the precipitation of mackinawite is focused on the zone of preferential flow. Secondary mineral precipitation may affect the hydraulic properties of this high permeability zone and may alter the flow distribution in the long term.

Conclusions

The conceptual model developed by *Bennett* [1997] was implemented into the numerical model MIN3P to describe the interactions between reaction and transport processes taking place at the reactive barrier in Elizabeth City, North Carolina. The simulation results agree well with the field observations. Processes downgradient of the barrier could only be investigated in a qualitative way, since data was not available and surface complexation reactions are not included in the present model.

The model allows visualization of important processes occurring in a reactive barrier composed of zero-valent iron. Processes such as the corrosion-reduction reactions and secondary mineral precipitation can be evaluated semi-quantitatively. The simulations provide estimates of iron corrosion rates from the sum of the reduction-corrosion reactions. The total accumulation and distribution of secondary precipitates can be estimated. Two-dimensional simulations highlight possibly adverse effects of preferential flow on contaminant treatment.

Discrepancies between the simulated *E*h conditions within the barrier and the field observations by *Bennett* [1997] illustrate that secondary reactions between the reduced reaction products, such as hydrogen gas, and the electron acceptors, which enter the barrier, may be important. The hypothesized reduction of sulfate by hydrogen gas may explain observed relatively low hydrogen gas concentrations. Degassing and the formation of hydrogen gas bubbles, which may affect the permeability and reactivity of the barrier, may be inhibited by this process.

More work is warranted to investigate reactive barriers for ground-water remediation and to study the long term performance of passive treatment systems. Possible model enhancements include the implementation of a more complete reaction network including secondary redox reactions, inhibition effects, surface complexation and effects of secondary mineral precipitation on the permeability and reactivity of the treatment material.

References

Allison, J. D., Brown, D. S. and Novo-Gradac, K. J. 1991. *MINTEQA2/PRODEFA2, A geochemical assessment model for environmental systems: Version 3.0 User's Manual*. U.S. Environmental Protection Agency, EPA/600/3-91/021.

Appelo, C. A. J., and Postma, D. 1993. *Geochemistry, groundwater and pollution*, A. A. Balkema, Rotterdam, Netherlands.

Bear, J. 1972. *Dynamics of fluids in porous media*, Elsevier Science, New York.

Bennett, T. A. 1997. An *in-situ* reactive barrier for the treatment of hexavalent chromium and trichloroethylene in groundwater, M.Sc. thesis, University of Waterloo, Waterloo, Ontario, Canada.

Blowes, D. W., Ptacek, C. J. and Jambor, J. L. 1997. *In-Situ* remediation of Cr(VI)-contaminated groundwater using permeable reactive walls: Laboratory studies, *Environ. Sci. Technol.*, 31(12), 3348-3357.

Blowes, D. W., Gillham, R. W. and Ptacek, C. J., Puls, R. W. 2000. An *in-situ* permeable reactive barrier for the treatment of hexavalent chromium and trichloroethylene in groundwater: Vol. 2. Performance monitoring, January, EPA/600/R-99/095b.

Carroll, S. A., and Walther, J. V. 1990. Kaolinite dissolution at 25°, 60°, and 80°, *Am. J. Sci.*, 290, 797-810.

Cheng, I. F., Muftikian, R., Fernando, Q. and Korte, N. 1997. Reduction of nitrate to ammonia by zero-valent iron, in *Proc. 213th ACS National Meeting*, Vol. 37, No. 1, 165-166, San Francisco, CA, American Chemical Society, Division of Environmental Chemistry.

Gould, J. P. 1982. The kinetics of hexavalent chromium reduction by metallic iron, *Water Res.*, 16, 871-877.

Kirkner, D. J., and Reeves, H. 1988. Multicomponent mass transport with homogeneous and heterogeneous chemical reactions: Effect of the chemistry on the choice of the numerical algorithm 1. Theory, *Water Resour. Res.*, 24(10), 1719-1729.

Klein, C., and Hurlbut Jr., C. S. 1993. *Manual of Mineralogy* (21 ed.), John Wiley & Sons, New York.

Lasaga, A. C. 1998. *Kinetic Theory in the Earth Sciences*, Princeton University Press, Princeton, New Jersey.

Lichtner, P. C. 1985. Continuum model for simultaneous chemical reactions and mass transport in hydrothermal systems, *Geochim. Cosmochim. Acta*, 49, 779-800.

Lichtner, P. C. 1996a. Continuum formulation of multicomponent-multiphase reactive transport, in Reactive Transport in Porous Media, edited by P. C. Lichtner, C. I. Steefel, and E. H. Oelkers, Vol. 34 of *Reviews in Mineralogy*, Mineralogical Society of America, Washington, DC.

Lichtner, P. C. 1996b. Modeling of reactive flow and transport in natural systems, in *Proceedings of the Rome Seminar on Environmental Geochemistry*, 5-72, Castelnuovo di Porto, May 22-26.

Lovley, D. R., and Goodwin, S. 1988. Hydrogen concentrations as an indicator of the predominant terminal electron-accepting reactions in aquatic sediments, *Geochim. Cosmochim. Acta*, 52, 2993-3003.

MacKenzie, P. D., Sivavec, T. M. and Horney, D. P. 1997. Mineral precipitation and porosity losses in iron treatment zones, in *Proc. 213th ACS National Meeting*, Vol. 37, No. 1, 154-157, San Francisco, CA, American Chemical Society, Division of Environmental Chemistry.

Mayer, K.U., 1999. A numerical model for multicomponent reactive transport in variably saturated porous media. Ph.D. thesis, Department of Earth Sciences, University of Waterloo, Waterloo, Ontario.

O'Hannesin, S. F., Hanton-Fong, C. J., Blowes, D. W., Gillham, R. W., and Ptacek, C.J. 1995. Remediation of groundwater contaminated with chromium and TCE using reactive barriers: Laboratory batch and column testing. Progress Report II for EPA - R.S. Kerr Environmental Research Lab, Waterloo Centre for Groundwater Research, University of Waterloo, Waterloo, Ontario, June.

Orth, W. S., and Gillham, R. W. 1996. Dechlorination of trichloroethene in aqueous solution using Fe^0, *Environ. Sci. Technol.*, 30(1), 66-71.

Palmer, C. D. 1999. Groundwater remediation using reactive barriers, Elizabeth City, NC site, Final Report to University of Waterloo, Department of Geology, Portland State University.

Powell, R. M., Puls, R. W., Hightower, S. K. and Sabatini, D. A. 1995. Coupled iron corrosion and chromate reduction: Mechanisms for subsurface remediation, *Environ. Sci. Technol.*, 29, 1913-1922.

Puls, R. W., Clark, D., Paul, C. J., and Vardy, J. 1992. Characterization of chromium contaminated soils and ground water in the vicinity of a chrome plating operation, in *Subsurface Restoration Conference. Third International Conference on Ground Water Quality Research*, 180-182, Dallas, Texas.

Puls, R. W., Powell, R. M., and Paul, C. J. 1995. In situ remediation of ground water contaminated with chromate and chlorinated solvents using zero-valent iron: A field study, in *Proc. 209th ACS National Meeting*, Vol. 35, No. 1, 788-791, Anaheim, CA, American Chemical Society, Division of Environmental Chemistry.

Puls, R. W., Rees, T. F., Lindley, P. M., and Paul, C. J. 1992. Surface analysis of chromium contaminated soils using scanning electron microscopy with energy dispersive X-ray (SEM-EDS) and secondary ion mass spectroscopy (SIMS), in *Subsurface Restoration Conference. Third International Conference on Ground Water Quality Research*, 125-127, Dallas, Texas.

Rahman, A., and Agrawal, A. 1997. Reduction of nitrate and nitrite by iron metal: Implications for groundwater remediation, in *Proc. 213th ACS National Meeting*, Vol. 37, No. 1, 157-159, San Francisco, CA, American Chemical Society, Division of Environmental Chemistry.

Reardon, E. J. 1995. Anaerobic corrosion of granular iron: Measurement and interpretation of hydrogen evolution rates, *Environ. Sci. Technol.*, 29(12), 2936-2945.

Sevougian, S. D., Schechter, R. S., and Lake, L. W. 1993. Effect of partial local equilibrium on the propagation of precipitation/dissolution waves, *Ind. Eng. Chem. Res.*, 32, 2281-2304.

Siantar, D. P., Schreier, C. G., and Reinhard, M. 1995. Transformation of the pesticide 1,2-dibromo-3-chloropropane (DBCP) and nitrate by iron powder and by H_2/Pd/Al_2O_3, in *Proc. 209th ACS National Meeting*, Vol. 35, No. 1, 745-748, Anaheim, CA, American Chemical Society, Division of Environmental Chemistry.

Steefel, C. I., and Lasaga, A. C. 1994. A coupled model for transport of multiple chemical species and kinetic precipitation/dissolution reactions with application to reactive flow in single phase hydrothermal systems, *Am. J. Sci.*, 294, 529-592.

Stumm, W., and Morgan, J. J. 1996. *Aquatic chemistry*, John Wiley & Sons, New York.

Unger, A. J. A., Sudicky, E. A., and Forsyth, P. A. 1995. Mechanisms controlling vacuum extraction coupled with air sparging for remediation of heterogeneous formations contaminated by dense non-aqueous phase liquids, *Water Resour. Res.*, 31(8), 1913-1925.

Weathers, L. J., Parkin, G. F., Nivak, P. J., and Alvarez, P. J. J. 1995. Methanogens couple anaerobic Fe(0) oxidation and $CHCl_3$ reduction, in *Proc. 209th ACS National Meeting*, Vol. 35, No. 1, 829-831, Anaheim, CA, American Chemical Society, Division of Environmental Chemistry.

Wolery, T. J., Jackson, K. J., Bourcier, W. L., Bruton, C. J., Viani, B. E., Knauss, K. G., and Delany, J. M. 1990. Current status of the EQ3/6 software package for geochemical modelling, in *Chemical Modeling of Aqueous Systems II*, edited by D. Melchior, and R. Bassett, Chapter 8, 105-116. Washington, D.C., USA, American Chemical Society.

Tables

Table 1. Complexation Reactions and Equilibrium Constants

Reaction			$\log K_i^x$
(1)	OH^-	$\rightleftharpoons H_2O - H^+$	-13.9980
(2)	$H_3SiO_4^-$	$\rightleftharpoons H_4SiO_4 - H^+$	-9.8300
(3)	$H_2SiO_4^{2-}$	$\rightleftharpoons H_4SiO_4 - 2H^+$	-23.0000
(4)	$NH_3(aq)$	$\rightleftharpoons NH_4^+ - H^+$	-9.2520
(5)	$NH_4SO_4^-$	$\rightleftharpoons NH_4^+ + SO_4^{2-}$	1.1100
(6)	$MgOH^+$	$\rightleftharpoons Mg^{2+} + H_2O - H^+$	-11.4400
(7)	$MgCO_3(aq)$	$\rightleftharpoons Mg^{2+} + CO_3^{2-}$	2.9800
(8)	$MgHCO_3^+$	$\rightleftharpoons Mg^{2+} + CO_3^{2-} + H^+$	11.4000
(9)	$MgSO_4(aq)$	$\rightleftharpoons Mg^{2+} + SO_4^{2-}$	2.3700
(10)	$CaOH^+$	$\rightleftharpoons Ca^{2+} + H_2O - H^+$	-12.7800
(11)	$CaHCO_3^+$	$\rightleftharpoons Ca^{2+} + CO_3^{2-} + H^+$	11.4400
(12)	$CaCO_3(aq)$	$\rightleftharpoons Ca^{2+} + CO_3^{2-}$	3.2200
(13)	$CaSO_4(aq)$	$\rightleftharpoons Ca^{2+} + SO_4^{2-}$	2.3090
(14)	$CaHSO_4^+$	$\rightleftharpoons Ca^{2+} + SO_4^{2-} + H^+$	3.0680
(15)	$NaCO_3^-$	$\rightleftharpoons Na^+ + CO_3^{2-}$	1.2680
(16)	$NaHCO_3(aq)$	$\rightleftharpoons Na^+ + CO_3^{2-} + H^+$	10.0800
(17)	$NaSO_4^-$	$\rightleftharpoons Na^+ + SO_4^{2-}$	0.7000
(18)	KSO_4^-	$\rightleftharpoons K^+ + SO_4^{2-}$	0.8500
(19)	$AlOH^{2+}$	$\rightleftharpoons Al^{3+} + H_2O - H^+$	-4.9900
(20)	$Al(OH)_2^+$	$\rightleftharpoons Al^{3+} + 2H_2O - 2H^+$	-10.1000
(21)	$Al(OH)_4^-$	$\rightleftharpoons Al^{3+} + 4H_2O - 4H^+$	-22.7000
(22)	$AlSO_4^+$	$\rightleftharpoons Al^{3+} + SO_4^{2-}$	3.5000
(23)	$AlHSO_4^{2+}$	$\rightleftharpoons Al^{3+} + SO_4^{2-} + H^+$	2.4480
(24)	$Al(SO4)_2^-$	$\rightleftharpoons Al^{3+} + 2SO_4^{2-}$	5.0000
(25)	$Al(OH)_3(aq)$	$\rightleftharpoons Al^{3+} + 3H_2O - 3H^+$	-16.9000
(26)	$FeOH^+$	$\rightleftharpoons Fe^{2+} + H_2O - H^+$	-9.5000
(27)	$Fe(OH)_3^-$	$\rightleftharpoons Fe^{2+} + 3H_2O - 3H^+$	-31.0000
(28)	$FeSO_4(aq)$	$\rightleftharpoons Fe^{2+} + SO_4^{2-}$	2.2500
(29)	$FeHSO_4^+$	$\rightleftharpoons Fe^{2+} + SO_4^{2-} + H^+$	3.0680
(30)	$FeHCO_3^+$	$\rightleftharpoons Fe^{2+} + CO_3^{2-} + H^+$	12.3300
(31)	$FeCO_3(aq)$	$\rightleftharpoons Fe^{2+} + O_3^{2-}$	4.3800
(32)	$Fe(OH)_2(aq)$	$\rightleftharpoons Fe^{2+} + 2H_2O - 2H^+$	-20.5700
(33)	$FeOH^{2+}$	$\rightleftharpoons Fe^{3+} + H_2O - H^+$	-2.1900

Table 1. Complexation Reactions and Equilibrium Constants - continued

Reaction			$\log K_i^x$
(34)	$FeSO_4^+$	$\rightleftharpoons Fe^{3+} + SO_4^{2-}$	4.0400
(35)	$FeHSO_4^{2+}$	$\rightleftharpoons Fe^{3+} + SO_4^{2-} + H^+$	4.4780
(36)	$FeCl^{2+}$	$\rightleftharpoons Fe^{3+} + Cl^-$	1.4800
(37)	$FeCl^+$	$\rightleftharpoons Fe^{2+} + Cl^-$	0.1400
(38)	$FeCl_2^+$	$\rightleftharpoons Fe^{3+} + 2Cl^-$	2.1300
(39)	$FeCl_3(aq)$	$\rightleftharpoons Fe^{3+} + 3Cl^-$	1.1300
(40)	$FeOH_2^+$	$\rightleftharpoons Fe^{3+} + 2H_2O - 2H^+$	-5.6700
(41)	$Fe(OH)_3(aq)$	$\rightleftharpoons Fe^{3+} + 3H_2O - 3H^+$	-12.5600
(42)	$Fe(OH)_4^-$	$\rightleftharpoons Fe^{3+} + 4H_2O - 4H^+$	-21.6000
(43)	$Fe(SO_4)_2^-$	$\rightleftharpoons Fe^{3+} + SO_4^{2-}$	5.3800
(44)	$Fe_2(OH)_2^{4+}$	$\rightleftharpoons Fe^{3+} + 2H_2O - 2H^+$	-2.9500
(45)	$Fe_3(OH)_4^{5+}$	$\rightleftharpoons Fe^{3+} + 4H_2O - 4H^+$	-6.3000
(46)	$MnCl^+$	$\rightleftharpoons Mn^{2+} + Cl^-$	0.6070
(47)	$MnCl_2(aq)$	$\rightleftharpoons Mn^{2+} + 2Cl^-$	0.2500
(48)	$MnCl_3^-$	$\rightleftharpoons Mn^{2+} + 3Cl^-$	-.3050
(49)	$MnOH^+$	$\rightleftharpoons Mn^{2+} + H_2O - H^+$	-10.5900
(50)	$Mn(OH)_3^-$	$\rightleftharpoons Mn^{2+} + 3H_2O - 3H^+$	-34.8000
(51)	$MnCO_3(aq)$	$\rightleftharpoons Mn^{2+} + CO_3^{2-}$	4.9000
(52)	$MnSO_4(aq)$	$\rightleftharpoons Mn^{2+} + SO_4^{2-}$	2.2600
(53)	$Mn(NO_3)_2(aq)$	$\rightleftharpoons Mn^{2+} + 2NO_3^-$	0.6000
(54)	$MnHCO_3^+$	$\rightleftharpoons Mn^{2+} + CO_3^{2-} + H^+$	12.2800
(55)	HCO_3^-	$\rightleftharpoons H^+ + CO_3^{2-}$	10.3300
(56)	$H2CO_3(aq)$	$\rightleftharpoons 2H^+ + CO_3^{2-}$	16.6810
(57)	HSO_4^-	$\rightleftharpoons H^+ + SO_4^{2-}$	1.9870
(58)	$H_2S_(aq)$	$\rightleftharpoons HS^- + H^+$	6.9940
(59)	S^{2-}	$\rightleftharpoons HS^- - H^+$	-12.9180
(60)	Cr^{3+}	$\rightleftharpoons Cr(OH)_2^+ + 2H^+ - 2H_2O$	9.6200
(61)	$CrOH^{2+}$	$\rightleftharpoons Cr(OH)_2^+ + H^+ - H_2O$	5.6200
(62)	$Cr(OH)_3(aq)$	$\rightleftharpoons Cr(OH)_2^+ - H^+ + H_2O$	-7.1300
(63)	$Cr(OH)_4^-$	$\rightleftharpoons Cr(OH)_2^+ - 2H^+ + 2H_2O$	-18.1500
(64)	CrO_2^-	$\rightleftharpoons Cr(OH)_2^+ - 2H^+$	-17.7456
(65)	$CrCl^{2+}$	$\rightleftharpoons Cr(OH)_2^+ + Cl^- + 2H^+ - 2H_2O$	9.3683
(66)	$CrCl_2^+$	$\rightleftharpoons Cr(OH)_2^+ + 2Cl^- + 2H^+ - 2H_2O$	8.6580

Table 1. Complexation Reactions and Equilibrium Constants - continued

Reaction			$\log K_i^x$
(67)	$CrOHCl_2(aq)$	$\rightleftharpoons Cr(OH)_2^+ + 2Cl^- + H^+ - H_2O$	2.9627
(68)	$CrNO_3^{2+}$	$\rightleftharpoons Cr(OH)_2^+ + NO_3^- + 2H^+ - 2H_2O$	8.2094
(69)	$CrSO_4^+$	$\rightleftharpoons Cr(OH)_2^+ + SO_4^{2-} + 2H^+ - 2H_2O$	10.9654
(70)	$CrOHSO_4(aq)$	$\rightleftharpoons Cr(OH)_2^+ + SO_4^{2-} + H^+ - H_2O$	8.2754
(71)	$Cr_2(OH)_2SO_4^{2+}$	$\rightleftharpoons 2Cr(OH)_2^+ + SO_4^{2-} + 2H^+ - 2H_2O$	16.1550
(72)	$Cr_2(OH)_2(SO_4)_2(aq)$	$\rightleftharpoons 2Cr(OH)_2^+ + 2SO_4^{2-} + 2H^+ - 2H_2O$	17.9288
(73)	$HCrO4^-$	$\rightleftharpoons CrO_4^{2-} + H^+$	6.5089
(74)	$H_2CrO_4(aq)$	$\rightleftharpoons CrO_4^{2-} + 2H^+$	5.6513
(75)	$Cr_2O_7^{2-}$	$\rightleftharpoons 2CrO_4^{2-} + 2H^+ - H_2O$	14.5571
(76)	CrO_3Cl^-	$\rightleftharpoons CrO_4^{2-} + Cl^- + 2H^+ - H_2O$	7.3086
(77)	$CrO_3SO_4^{2-}$	$\rightleftharpoons CrO_4^{2-} + SO_4^{2-} + 2H^+ - H_2O$	8.9937
(78)	$NaCrO_4^-$	$\rightleftharpoons Na^+ + CrO_4^{2-}$	0.6963
(79)	$KCrO_4^-$	$\rightleftharpoons K^+ + CrO_4^{2-}$	0.7990

Table 2. Reaction Stoichiometries of Reduction-corrosion Reactions

Oxidant	Reaction
Cr(VI)	$Fe^0(s) + CrO_4^{2-} + 6H^+ \rightarrow Fe^{3+} + Cr(OH)_2^+ + 2H_2O$
TCE	$Fe^0(s) + 0.3025\ C_2HCl_3 + 1.2325H^+ \rightarrow$
	$Fe^{2+} + 0.07\ C_2H_2Cl_2 + 0.2325\ C_2H_6 + 0.7675\ Cl^-$
cis-1,2 DCE	$Fe^0(s) + C_2H_2Cl_2 + H^+ \rightarrow Fe^{2+} + C_2H_3Cl + Cl^-$
VC	$Fe^0(s) + \frac{1}{2}C_2H_3Cl + \frac{3}{2}H^+ \rightarrow Fe^{2+} + \frac{1}{2}C_2H_6 + \frac{1}{2}Cl^-$
oxygen	$Fe^0(s) + \frac{1}{4}O_2(aq) + 3H^+ \rightarrow Fe^{3+} + \frac{1}{2}H_2O + H_2(aq)$
nitrate	$Fe^0(s) + \frac{3}{8}NO_3^- + \frac{15}{4}H^+ \rightarrow Fe^{3+} + \frac{3}{8}NH_4^+ + \frac{9}{8}H_2O$
sulfate	$Fe^0(s) + \frac{1}{4}SO_4^{2-} + \frac{9}{4}H^+ \rightarrow Fe^{2+} + \frac{1}{4}HS^- + H_2O$
DOC	$Fe^0(s) + \frac{1}{2}CH_2O + 2H^+ \rightarrow Fe^{2+} + \frac{1}{2}CH_4(aq) + \frac{1}{2}H_2O$
DIC	$Fe^0(s) + \frac{1}{4}CO_3^{2-} + \frac{5}{2}H^+ \rightarrow Fe^{2+} + \frac{1}{4}CH_4(aq) + \frac{3}{4}H_2O$
water	$Fe^0(s) + 2H^+ \rightarrow Fe^{2+} + H_2(aq)$

Table 3. Secondary Minerals in Reactive Barrier and Corresponding Equilibrium Constants

Reaction		$\log K$
$Fe(OH)_2(am)$	$\rightleftharpoons Fe^{2+} + 2H_2O - 2H^+$	-13.9045
$Fe(OH)_3(am)$	$\rightleftharpoons Fe^{3+} + 3H_2O - 3H^+$	-4.8910
$Cr(OH)_3(am)$	$\rightleftharpoons Cr^{3+} + 3H_2O - 3H^+$	0.7500
$CaCO_3(s)$	$\rightleftharpoons Ca^{2+} + CO_3^{2-}$	8.4750
$CaMg(CO_3)_2(s)$	$\rightleftharpoons Ca^{2+} + Mg^{2+} + 2CO_3^{2-}$	17.0900
$FeCO_3(s)$	$\rightleftharpoons Fe^{2+} + CO_3^{2-}$	10.4500
$MnCO_3(s)$	$\rightleftharpoons Mn^{2+} + CO_3^{2-}$	10.4100
$FeS(am)$	$\rightleftharpoons Fe^{2+} + HS^- - H^+$	4.6480

Table 4. Physical Parameters for Aquifer and Reactive Barrier Material

parameter	unit	
hydraulic conductivity (1-D)	$[m\ s^{-1}]$	$8.1 \cdot 10^{-5} - 1.2 \cdot 10^{-3}$
hydraulic conductivity (2-D)	$[m\ s^{-1}]$	$1.2 \cdot 10^{-6} - 1.2 \cdot 10^{-3}$
hydraulic gradient (average)	[-]	$2.2 \cdot 10^{-3}$
porosity (aquifer)	[-]	0.38
porosity (reactive barrier)	[-]	0.5

Table 5. Initial Mineral Volume Fractions in Reactive Barrier and Aquifer

	Mineral	volume fraction	Reference
Reactive barrier	$Fe^0(s)$	0.5 - 0.62	*Bennett* [1997]
Aquifer	goethite	$1.0 \cdot 10^{-3}$	estimated
	pyrolusite	$1.0 \cdot 10^{-3}$	estimated
	non-reactive	0.698	estimated

Table 6. Reactive Surface Area Estimates for Zero Valent-iron (Field Installation)

surface area $[m^2$ mineral m^{-3} mineral$]$	
geometric surface area (calculated from $d_{50} = 0.4$ mm)	$7.50 \cdot 10^3$
specific reactive surface area (calculated from laboratory experiment)	$3.88 \cdot 10^6$

Table 7. Reactive Surface Area Estimates for Eh-buffer Minerals

mineral	reactive surface area
goethite	$1.0 \cdot 10^{2}$
pyrolusite	$1.0 \cdot 10^{2}$

Table 8. Input Concentrations at Boundary Located Upgradient of Reactive Barrier, Transect 2, 21-1 - 21-4

		21-1	21-2	21-3	21-4
depth	[m]	7.0	6.5	6.0	5.5
pH	[-]	7.36	7.84	7.97	6.40
E_{H}	[mV]	377	441	356	437
CO_3^{2-}	[mol l^{-1}]	$1.13 \cdot 10^{-03}$	$1.23 \cdot 10^{-03}$	$1.22 \cdot 10^{-03}$	$1.85 \cdot 10^{-03}$
Cl^-	[mol l^{-1}]	$4.23 \cdot 10^{-04}$	$5.87 \cdot 10^{-04}$	$8.44 \cdot 10^{-04}$	$2.33 \cdot 10^{-03}$
SO_4^{2-}	[mol l^{-1}]	$1.91 \cdot 10^{-04}$	$3.28 \cdot 10^{-04}$	$5.30 \cdot 10^{-04}$	$9.38 \cdot 10^{-04}$
HS^-	[mol l^{-1}]	$5.54 \cdot 10^{-88}$	$8.00 \cdot 10^{-100}$	$3.80 \cdot 10^{-90}$	$2.52 \cdot 10^{-86}$
NO_3^-	[mol l^{-1}]	$1.18 \cdot 10^{-05}$	$1.16 \cdot 10^{-05}$	$1.08 \cdot 10^{-05}$	$4.61 \cdot 10^{-05}$
NH_4^+	[mol l^{-1}]	$3.72 \cdot 10^{-11}$	$1.32 \cdot 10^{-24}$	$2.72 \cdot 10^{-14}$	$4.44 \cdot 10^{-09}$
Na^+	[mol l^{-1}]	$8.96 \cdot 10^{-04}$	$1.54 \cdot 10^{-03}$	$2.19 \cdot 10^{-03}$	$3.64 \cdot 10^{-03}$
K^+	[mol l^{-1}]	$2.05 \cdot 10^{-05}$	$4.35 \cdot 10^{-05}$	$2.05 \cdot 10^{-05}$	$4.86 \cdot 10^{-05}$
Ca^{2+}	[mol l^{-1}]	$2.77 \cdot 10^{-04}$	$2.22 \cdot 10^{-04}$	$1.96 \cdot 10^{-04}$	$3.92 \cdot 10^{-04}$
Mg^{2+}	[mol l^{-1}]	$2.69 \cdot 10^{-04}$	$2.06 \cdot 10^{-04}$	$1.81 \cdot 10^{-04}$	$4.20 \cdot 10^{-04}$
Fe^{2+}	[mol l^{-1}]	$1.69 \cdot 10^{-15}$	$5.56 \cdot 10^{-18}$	$6.84 \cdot 10^{-17}$	$1.42 \cdot 10^{-13}$
Fe^{3+}	[mol l^{-1}]	$1.20 \cdot 10^{-12}$	$1.03 \cdot 10^{-12}$	$1.03 \cdot 10^{-12}$	$3.81 \cdot 10^{-12}$
CrO_4^{2-}	[mol l^{-1}]	$5.78 \cdot 10^{-08}$	$1.93 \cdot 10^{-05}$	$3.71 \cdot 10^{-05}$	$4.75 \cdot 10^{-05}$
$Cr(OH)_2^+$	[mol l^{-1}]	$2.16 \cdot 10^{-08}$	$1.60 \cdot 10^{-08}$	$1.53 \cdot 10^{-08}$	$1.11 \cdot 10^{-07}$
Mn^{2+}	[mol l^{-1}]	$1.77 \cdot 10^{-06}$	$1.57 \cdot 10^{-06}$	$2.04 \cdot 10^{-06}$	$5.97 \cdot 10^{-06}$
Al^{3+}	[mol l^{-1}]	$3.88 \cdot 10^{-08}$	$1.15 \cdot 10^{-07}$	$1.55 \cdot 10^{-07}$	$8.07 \cdot 10^{-09}$
H_4SiO_4	[mol l^{-1}]	$9.43 \cdot 10^{-06}$	$9.50 \cdot 10^{-06}$	$9.54 \cdot 10^{-06}$	$9.40 \cdot 10^{-06}$
$O_2(aq)$	[mol l^{-1}]	$9.13 \cdot 10^{-05}$	$3.72 \cdot 10^{-05}$	$6.25 \cdot 10^{-06}$	$1.56 \cdot 10^{-05}$
$H_2(aq)$	[mol l^{-1}]	$2.57 \cdot 10^{-31}$	$1.93 \cdot 10^{-34}$	$8.63 \cdot 10^{-32}$	$2.00 \cdot 10^{-31}$
TCE	[mol l^{-1}]	$2.04 \cdot 10^{-05}$	$3.27 \cdot 10^{-06}$	$2.82 \cdot 10^{-07}$	$2.59 \cdot 10^{-07}$
cis-1,2 DCE	[mol l^{-1}]	$5.16 \cdot 10^{-09}$	$5.16 \cdot 10^{-09}$	$5.16 \cdot 10^{-09}$	$9.29 \cdot 10^{-09}$
VC	[mol l^{-1}]	$8.00 \cdot 10^{-09}$	$8.00 \cdot 10^{-09}$	$8.00 \cdot 10^{-09}$	$8.00 \cdot 10^{-09}$
ethane	[mol l^{-1}]	$1.66 \cdot 10^{-07}$	$1.66 \cdot 10^{-07}$	$1.66 \cdot 10^{-07}$	$1.66 \cdot 10^{-07}$
CH_2O	[mol l^{-1}]	$1.37 \cdot 10^{-04}$	$6.99 \cdot 10^{-06}$	$4.84 \cdot 10^{-05}$	$3.55 \cdot 10^{-05}$
$CH_4(aq)$	[mol l^{-1}]	$4.80 \cdot 10^{-06}$	$1.75 \cdot 10^{-06}$	$3.86 \cdot 10^{-06}$	$3.37 \cdot 10^{-06}$

Table 9. Input Concentrations at Boundary Located Upgradient of Reactive Barrier, Transect 2, 21-5 - 21-7

		21-5	21-6	21-7
depth	[m]	5.0	4.5	4.0
pH	[-]	6.29	6.48	6.94
E_{H}	[mV]	444	441	385
CO_3^{2-}	[mol l^{-1}]	$1.95 \cdot 10^{-03}$	$2.98 \cdot 10^{-03}$	$2.40 \cdot 10^{-03}$
Cl^-	[mol l^{-1}]	$4.04 \cdot 10^{-03}$	$1.98 \cdot 10^{-03}$	$7.36 \cdot 10^{-04}$
SO_4^{2-}	[mol l^{-1}]	$1.44 \cdot 10^{-03}$	$3.24 \cdot 10^{-04}$	$8.40 \cdot 10^{-05}$
HS^-	[mol l^{-1}]	$5.29 \cdot 10^{-86}$	$4.03 \cdot 10^{-88}$	$1.86 \cdot 10^{-85}$
NO_3^-	[mol l^{-1}]	$8.83 \cdot 10^{-05}$	$2.69 \cdot 10^{-05}$	$3.69 \cdot 10^{-06}$
NH_4^+	[mol l^{-1}]	$1.35 \cdot 10^{-08}$	$1.18 \cdot 10^{-10}$	$1.77 \cdot 10^{-08}$
Na^+	[mol l^{-1}]	$6.01 \cdot 10^{-03}$	$1.78 \cdot 10^{-03}$	$7.92 \cdot 10^{-04}$
K^+	[mol l^{-1}]	$6.65 \cdot 10^{-05}$	$1.25 \cdot 10^{-04}$	$1.48 \cdot 10^{-04}$
Ca^{2+}	[mol l^{-1}]	$5.32 \cdot 10^{-04}$	$6.86 \cdot 10^{-04}$	$5.47 \cdot 10^{-04}$
Mg^{2+}	[mol l^{-1}]	$5.97 \cdot 10^{-04}$	$6.38 \cdot 10^{-04}$	$4.36 \cdot 10^{-04}$
Fe^{2+}	[mol l^{-1}]	$2.53 \cdot 10^{-13}$	$6.91 \cdot 10^{-14}$	$2.48 \cdot 10^{-14}$
Fe^{3+}	[mol l^{-1}]	$4.71 \cdot 10^{-12}$	$3.30 \cdot 10^{-12}$	$1.71 \cdot 10^{-12}$
CrO_4^{2-}	[mol l^{-1}]	$9.84 \cdot 10^{-05}$	$8.93 \cdot 10^{-06}$	$2.89 \cdot 10^{-08}$
$Cr(OH)_2^+$	[mol l^{-1}]	$1.52 \cdot 10^{-07}$	$8.93 \cdot 10^{-08}$	$3.64 \cdot 10^{-08}$
Mn^{2+}	[mol l^{-1}]	$7.88 \cdot 10^{-06}$	$2.13 \cdot 10^{-05}$	$4.37 \cdot 10^{-05}$
Al^{3+}	[mol l^{-1}]	$8.17 \cdot 10^{-09}$	$8.38 \cdot 10^{-09}$	$1.62 \cdot 10^{-08}$
H_4SiO_4	[mol l^{-1}]	$9.40 \cdot 10^{-06}$	$9.40 \cdot 10^{-06}$	$9.40 \cdot 10^{-06}$
$O_2(aq)$	[mol l^{-1}]	$8.13 \cdot 10^{-06}$	$1.06 \cdot 10^{-05}$	$2.47 \cdot 10^{-05}$
$H_2(aq)$	[mol l^{-1}]	$1.98 \cdot 10^{-31}$	$1.01 \cdot 10^{-31}$	$9.91 \cdot 10^{-31}$
TCE	[mol l^{-1}]	$1.98 \cdot 10^{-06}$	$2.29 \cdot 10^{-06}$	$4.72 \cdot 10^{-07}$
cis-1,2 DCE	[mol l^{-1}]	$1.37 \cdot 10^{-06}$	$2.95 \cdot 10^{-06}$	$5.73 \cdot 10^{-07}$
VC	[mol l^{-1}]	$1.73 \cdot 10^{-07}$	$1.05 \cdot 10^{-06}$	$1.23 \cdot 10^{-06}$
ethane	[mol l^{-1}]	$2.99 \cdot 10^{-06}$	$1.66 \cdot 10^{-07}$	$1.66 \cdot 10^{-07}$
CH_2O	[mol l^{-1}]	$7.78 \cdot 10^{-05}$	$1.01 \cdot 10^{-04}$	$4.98 \cdot 10^{-05}$
$CH_4(aq)$	[mol l^{-1}]	$1.37 \cdot 10^{-06}$	$9.29 \cdot 10^{-06}$	$1.35 \cdot 10^{-05}$

Table 10. Reaction Processes Affecting Component Concentrations

component	sources	sinks
CO_3^{2-}	-	carbonate minerals
		DIC-reduction
Cl^-	-	-
SO_4^{2-}	-	sulfate reduction
HS^-	sulfate reduction	mackinawite
NO_3^-	-	nitrate reduction
NH_4^+	nitrate reduction	-
Na^+	-	-
K^+	-	-
Ca^{2+}	-	calcite, Ca-Mg-carbonate
Mg^{2+}	-	Ca-Mg-carbonate
Fe^{2+}	iron corrosion	siderite, $Fe(OH)_2$,
	goethite	mackinawite
Fe^{3+}	iron corrosion	$Fe(OH)_3$
CrO_4^{2-}	-	Cr(VI)-reduction
$Cr(OH)_2^+$	Cr(VI)-reduction	$Cr(OH)_3$
Mn^{2+}	pyrolusite	rhodocrosite
Al^{3+}	-	-
H_4SiO_4	-	-
O_2(aq)	-	O_2-reduction
H_2(aq)	iron corrosion	-
TCE	-	TCE-reduction
cis-1,2 DCE	TCE-reduction	cis-1,2 DCE-reduction
VC	cis-1,2 DCE-reduction	VC-reduction
ethane	TCE- and VC-reduction	-
CH_2O	-	DOC-reduction
CH_4(aq)	DIC- and DOC-reduction	-
pH	reduction-corrosion reactions	
	secondary mineral formation	
	deprotonation	
E_H	reduction-corrosion reactions	
	secondary mineral formation	

Table 11. Rate Constants for Reduction-corrosion Reactions

oxidant	log k calibrated	log k lab data	unit	reference
Cr(VI)	2.895	2.895	[l m^{-2} d^{-1}]	*Gould* [1982]
TCE	-2.207	-2.207	[l m^{-2} d^{-1}]	*O'Hannesin et al.* [1995]
cis-1,2 DCE	-3.179	-3.179	[l m^{-2} d^{-1}]	*O'Hannesin et al.* [1995]
VC	-2.383	-2.383	[l m^{-2} d^{-1}]	*O'Hannesin et al.* [1995]
oxygen	2.5	-	[l m^{-2} d^{-1}]	-
nitrate	-1.589	-2.589	[l m^{-2} d^{-1}]	*Rahman and Agrawal* [1997][1)]
sulfate	-2.5	-	[l m^{-2} d^{-1}]	-
DOC	-3.8	-	[l m^{-2} d^{-1}]	-
DIC	-3.8	-	[l m^{-2} d^{-1}]	-
water	-10.331	-6.331	[mol m^{-2} d^{-1}]	*Reardon* [1995][2)]

1) calculated based on surface area estimated from grain size
2) calculated based on measured surface area

Table 12. Calibrated Effective Rate Constants for Secondary Mineral Formation

mineral	log k_{eff} [mol m^{-3} d^{-1}]
$Fe(OH)_2(am)$	-1.000
$Fe(OH)_3(am)$	-1.000
$Cr(OH)_3(am)$	-2.000
$CaCO_3(s)$	-1.200
$CaMg(CO_3)_2(s)$	-2.500
$FeCO_3(s)$	-2.000
$MnCO_3(s)$	-2.500
FeS(am)	-2.000

Table 13. Estimated Rate Constants for Reductive Dissolution Reactions

mineral	log k [mol m^{-2} d^{-1}]
FeOOH(s)	-5.000
$MnO_2(s)$	-5.000

Figures

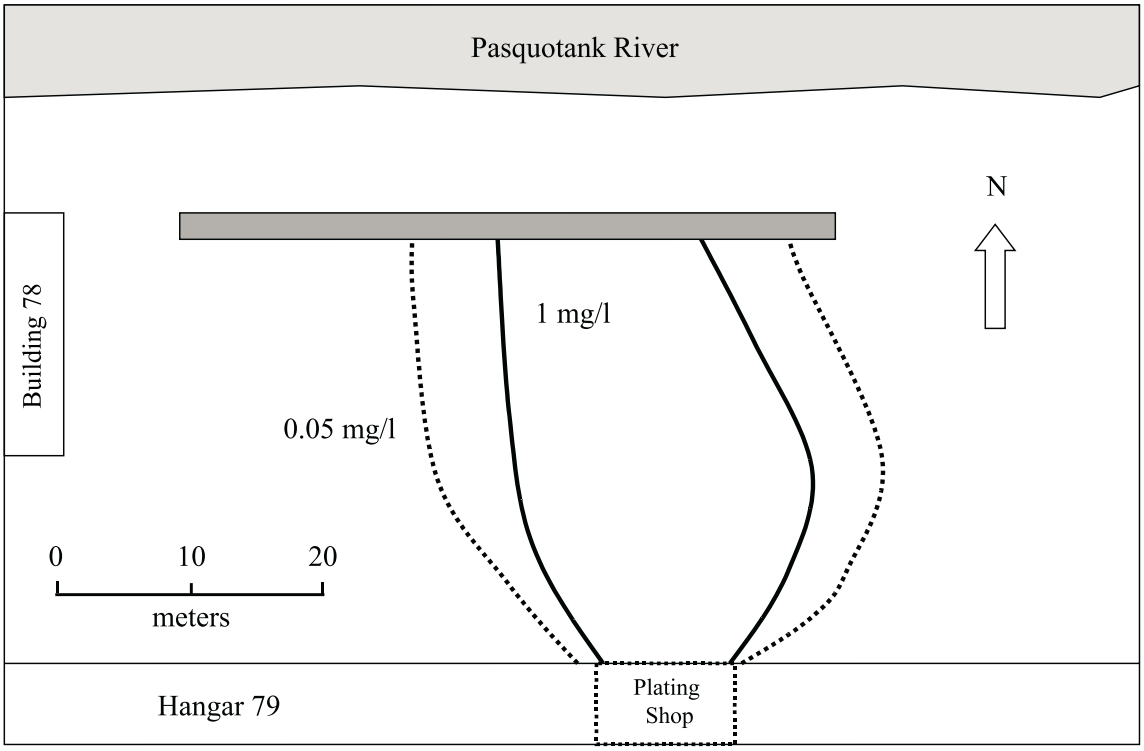

Figure 1. Configuration of reactive barrier and approximate location of chromium plume, from Bennett [1997].

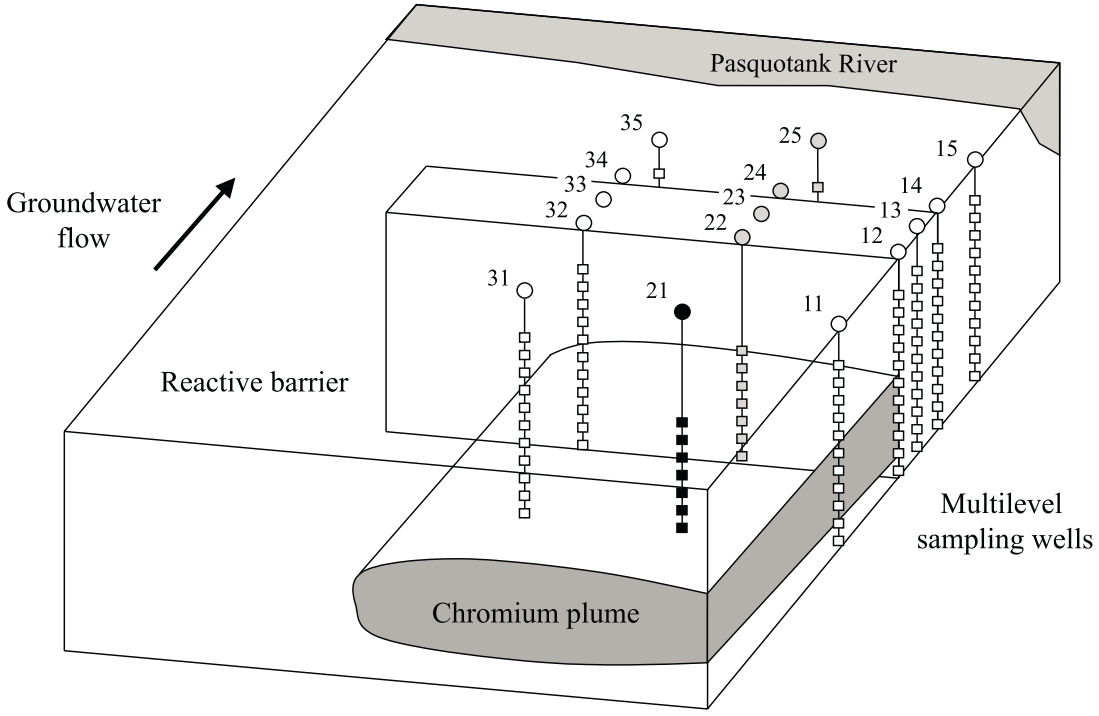

Figure 2. Monitoring network, from Bennett [1997].

Contaminated Zone	Treatment Zone	Buffer Zone
Advective-dispersive transport of contaminants and other dissolved species	Removal of contaminants by reduction and precipitation Reduction of other Corrosion of zero-valent iron pH-*increase* Eh-*decrease* Precipitation of secondary minerals Exsolution of dissolved gases pH and Eh buffering	Dissolution of clay minerals Desorption of hydrogen ions pH - *decrease* Reductive dissolution of oxides and oxy-hydroxides Exsolution of dissolved gases Eh-*increase*
upgradient	**reactive barrier**	**downgradient**

Figure 3. Conceptual model for reactive barriers comprised of zero-valent iron, from Bennett [1997].

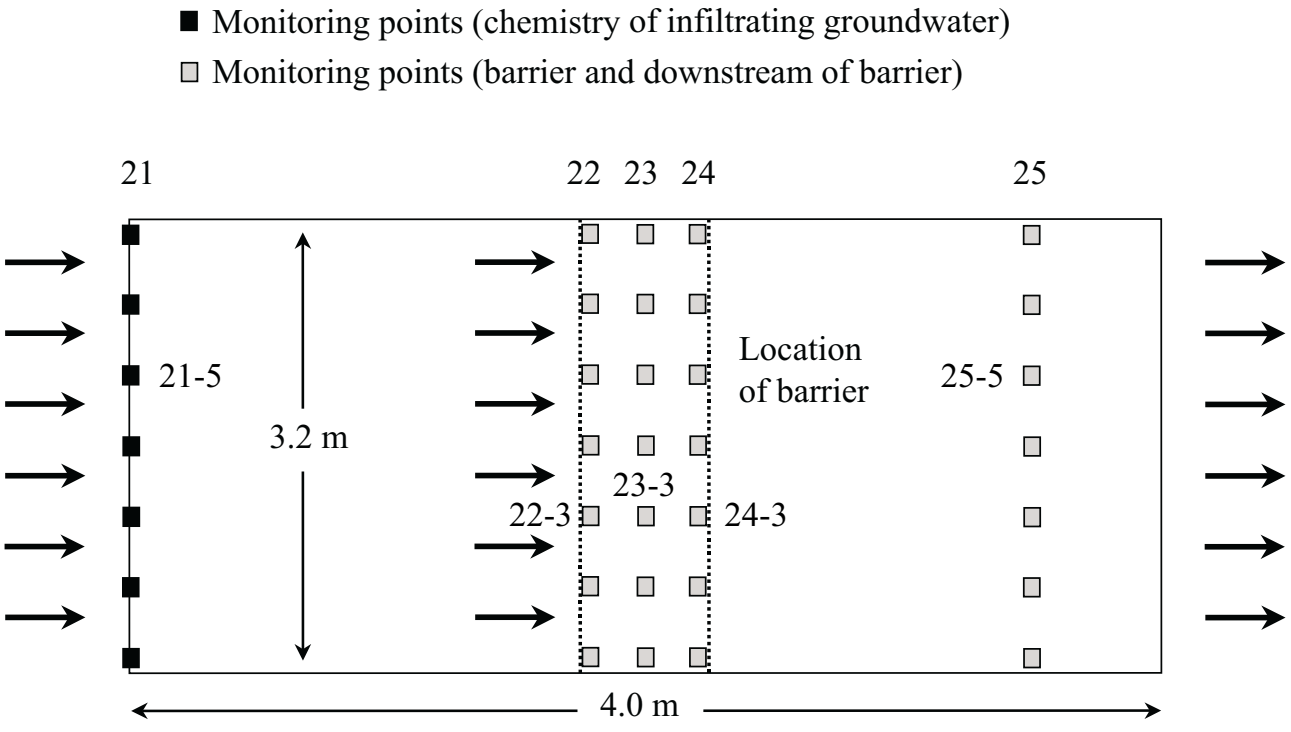

Figure 4. Solution domain including location of barrier and monitoring points along Transect 2.

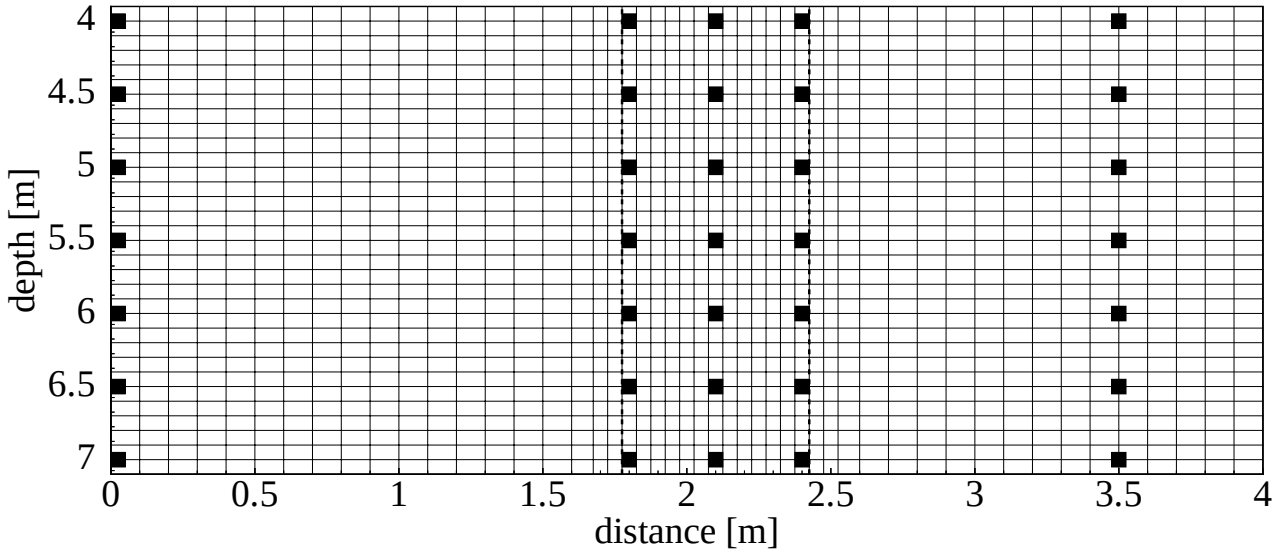

Figure 5. Spatial discretization of two-dimensional solution domain.

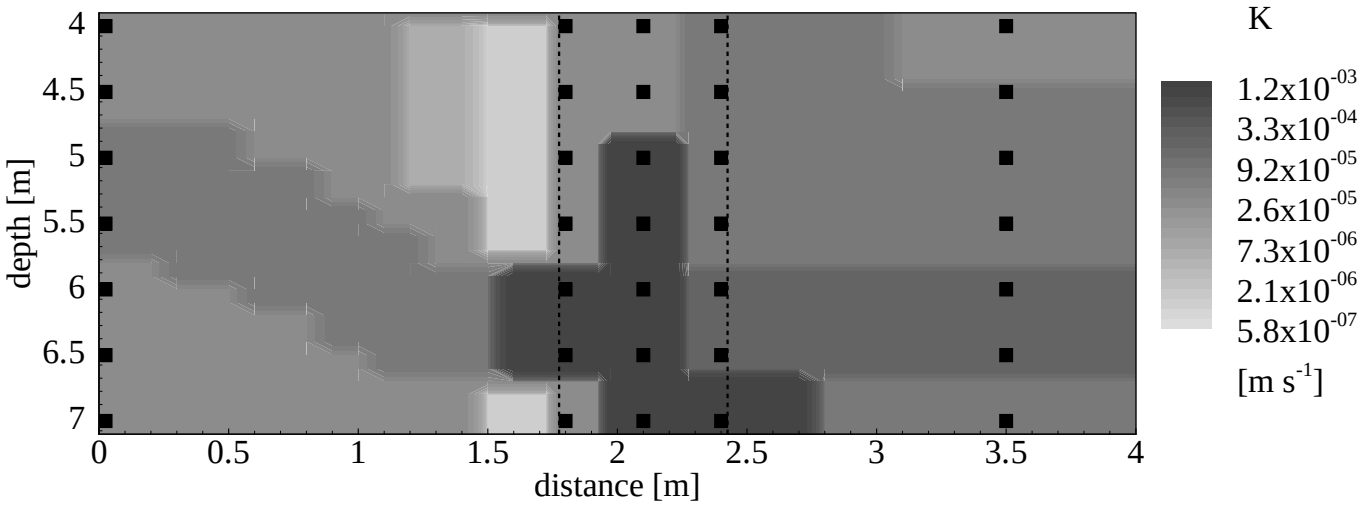

Figure 6. Hydraulic conductivity distribution in two-dimensional solution domain, modified from Bennett [1997].

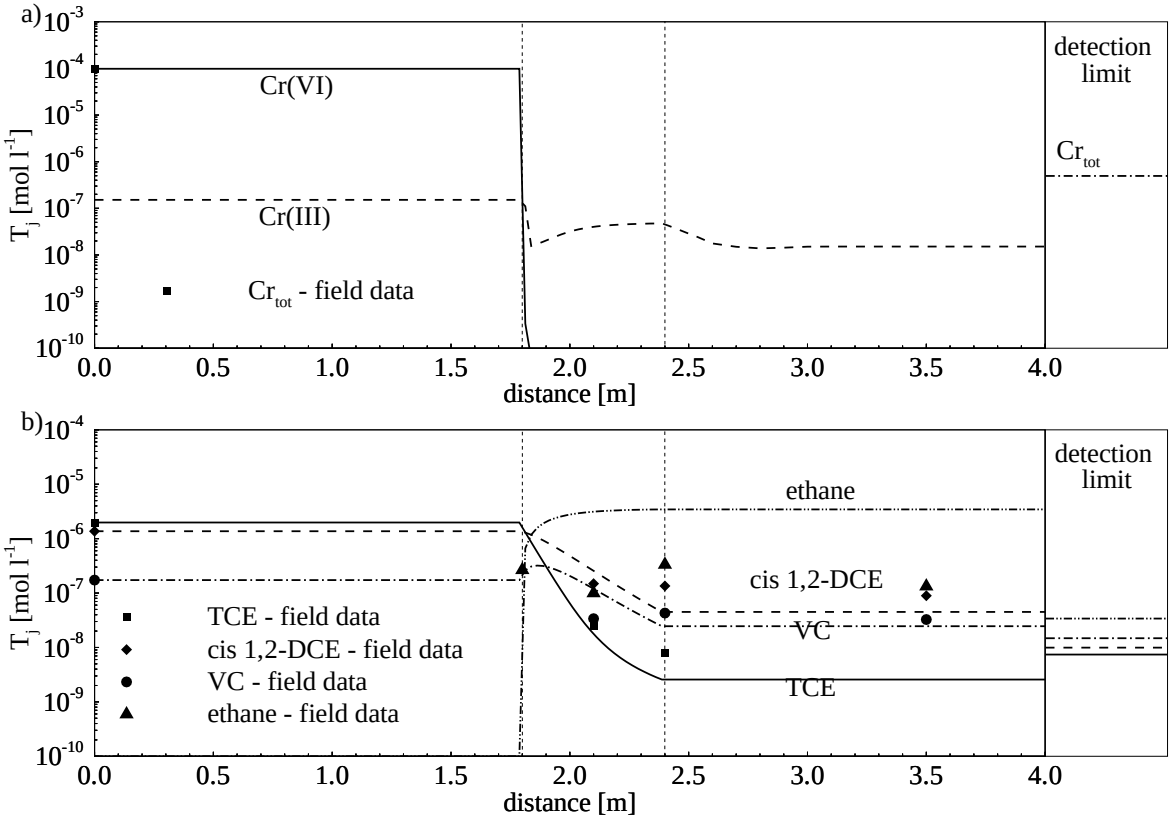

Figure 7. Contaminant concentrations after t = 240 days: a) chromium, b) organics - one-dimensional simulation.

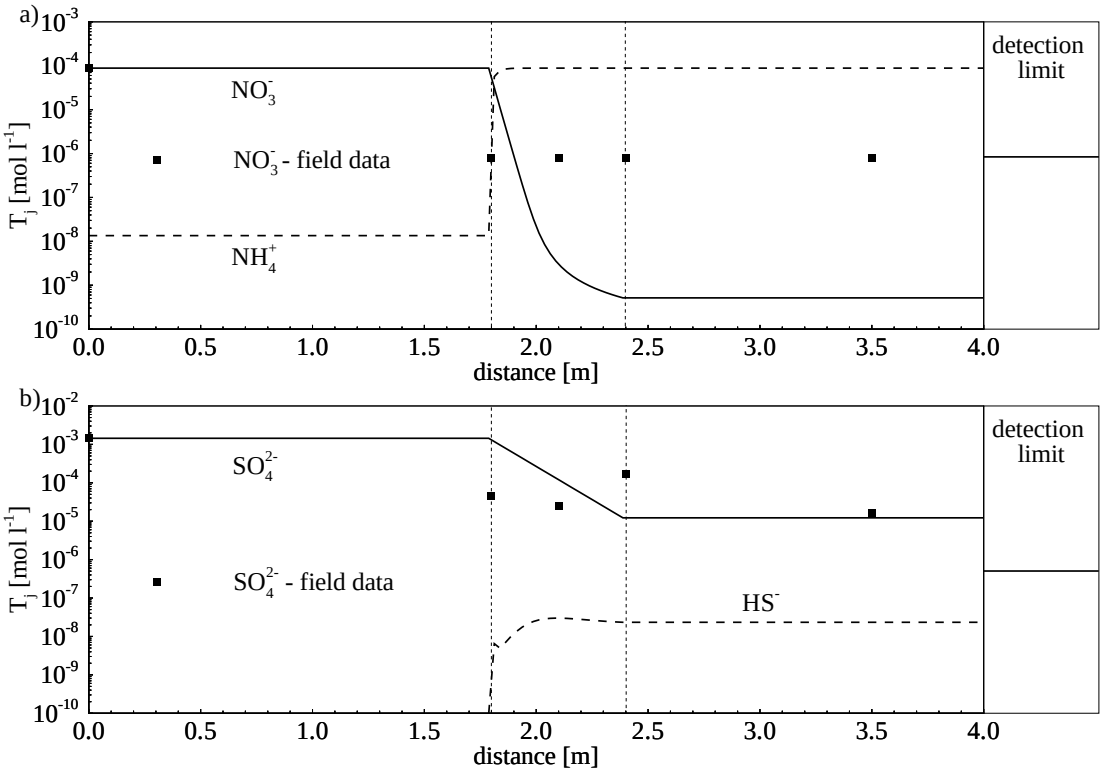

Figure 8. Redox couple concentrations after t = 240 days: a) nitrate/ammonia, b) sulfate/sulfide - one-dimensional simulation.

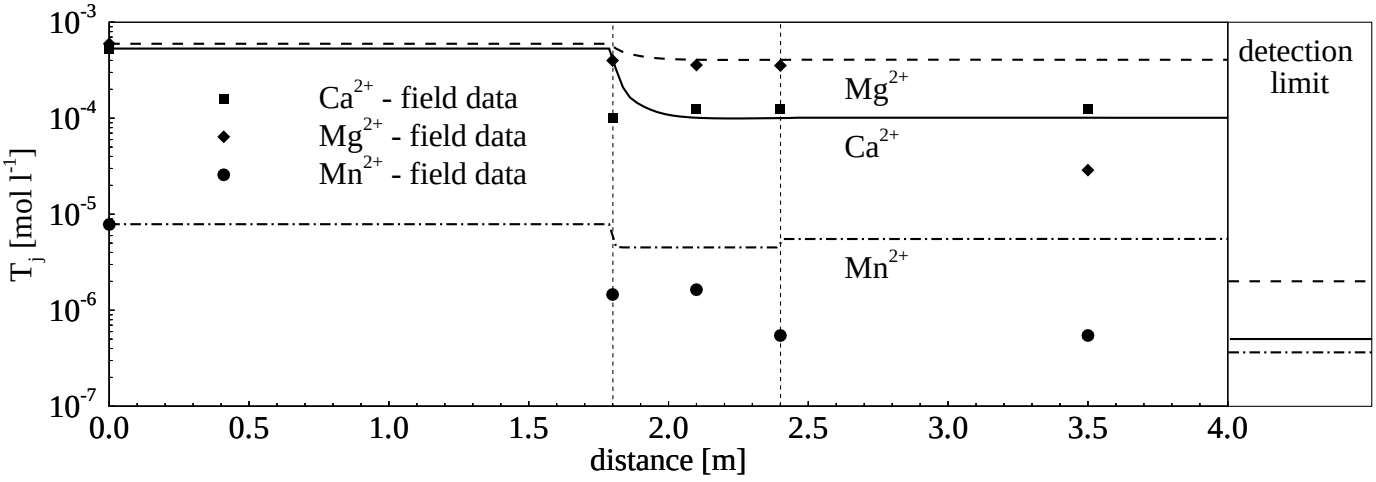

Figure 9. Selected cation concentrations after t = 240 days - one-dimensional simulation.

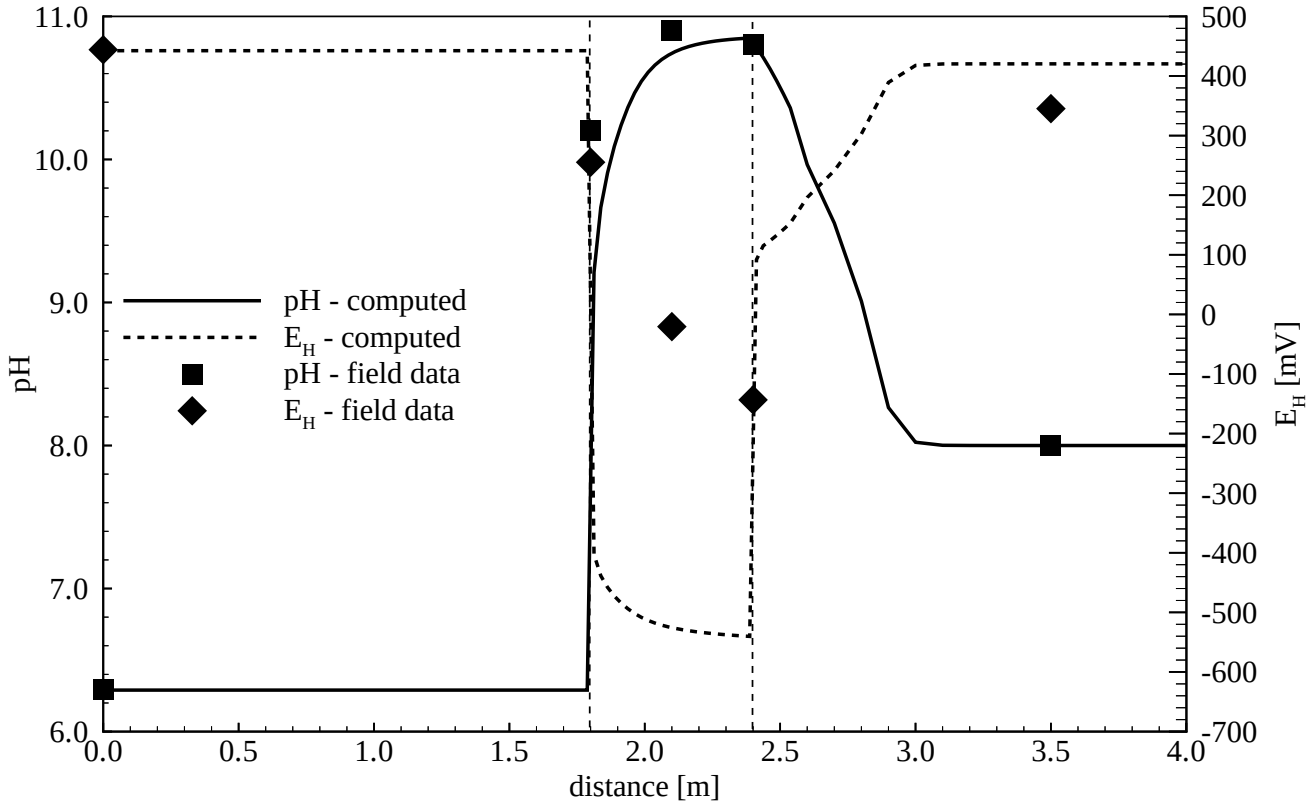

Figure 10. pH and Eh after t = 240 days - one-dimensional simulation.

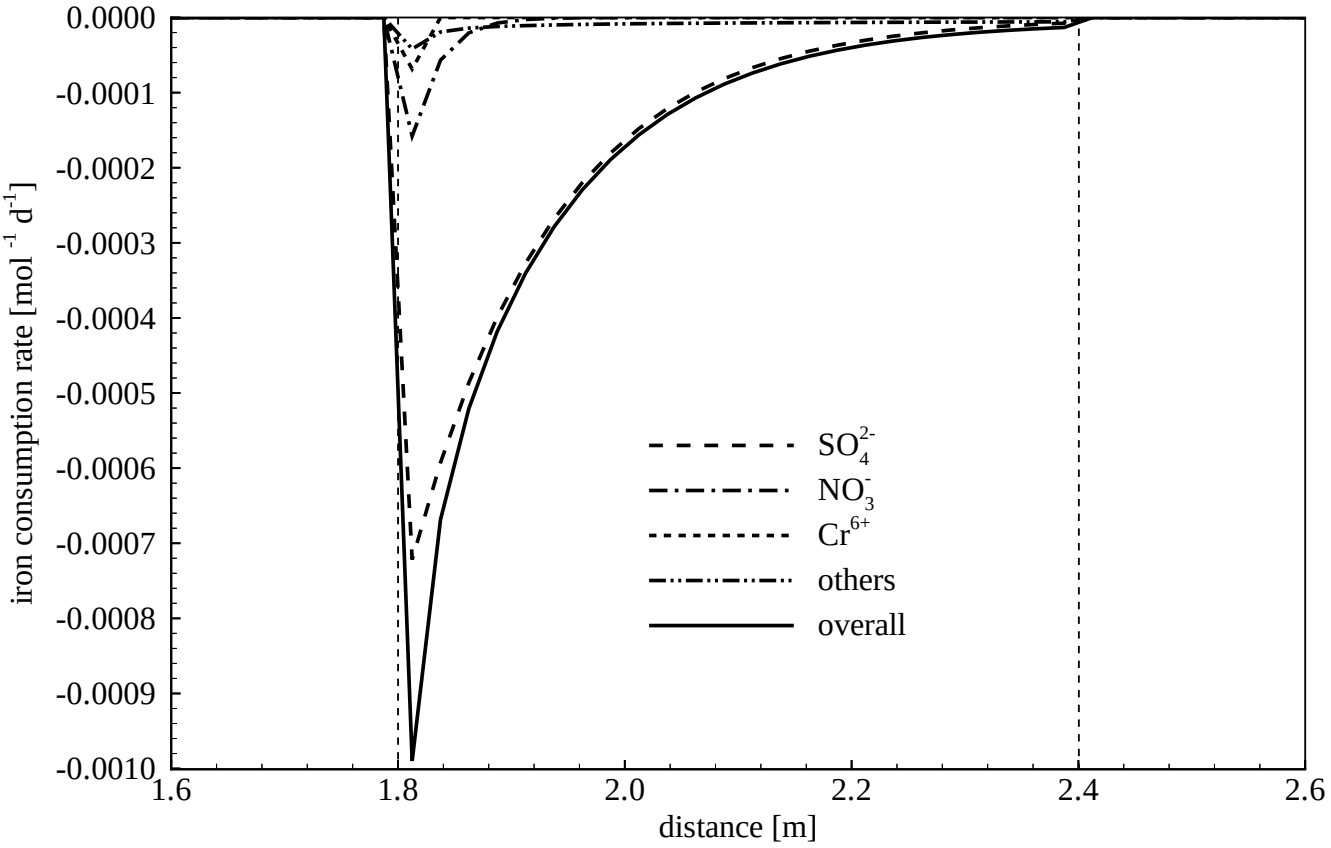

Figure 11. Iron corrosion rates in reactive barrier after t = 240 days.

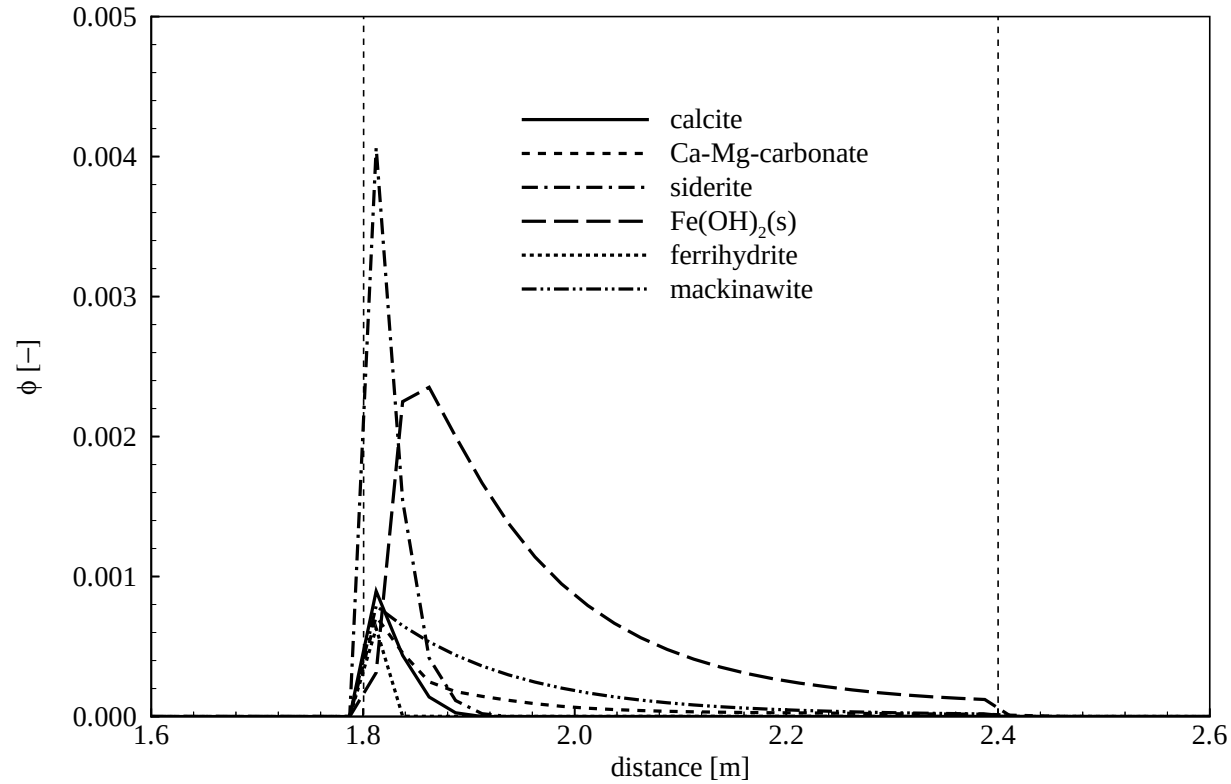

Figure 12. Secondary mineral volume fractions in reactive barrier after t = 240 days.

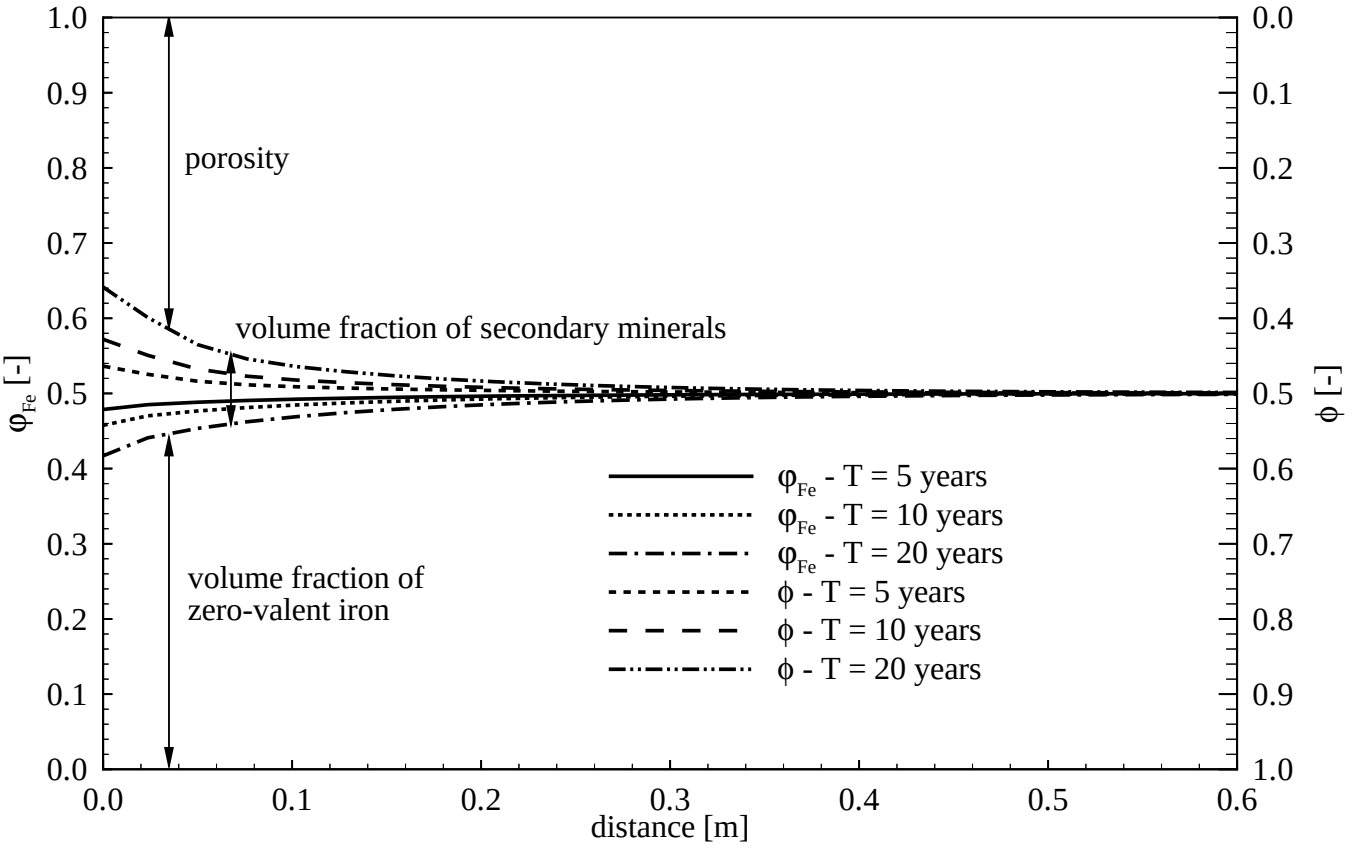

Figure 13. Long term effect of iron corrosion and secondary mineral formation.

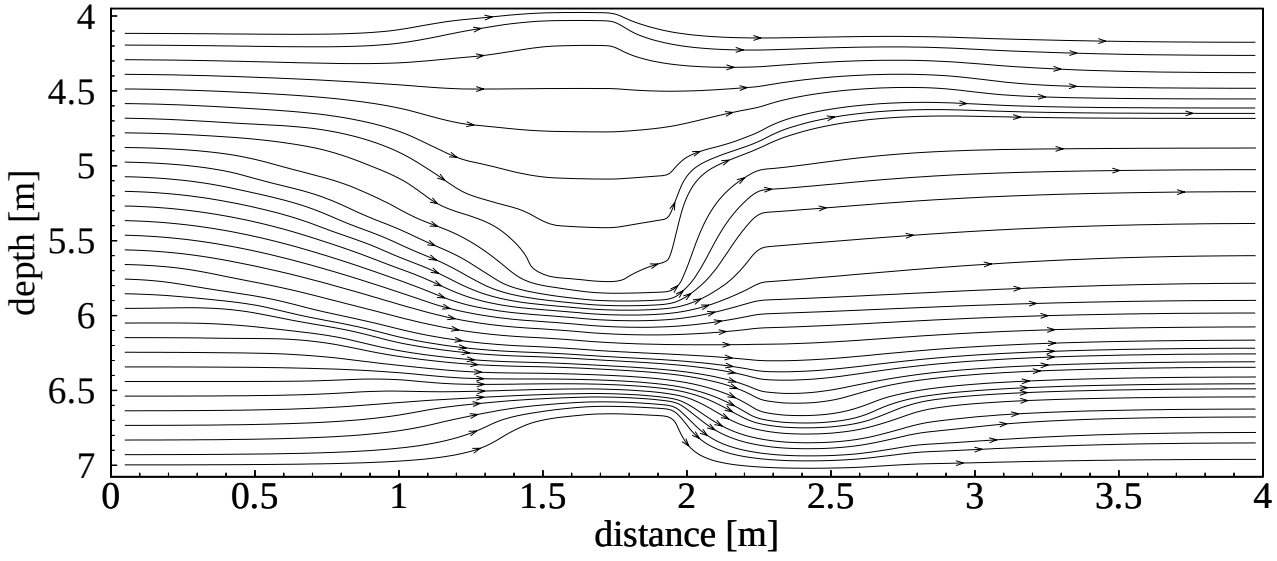

Figure 14. Streamlines in two-dimensional solution domain.

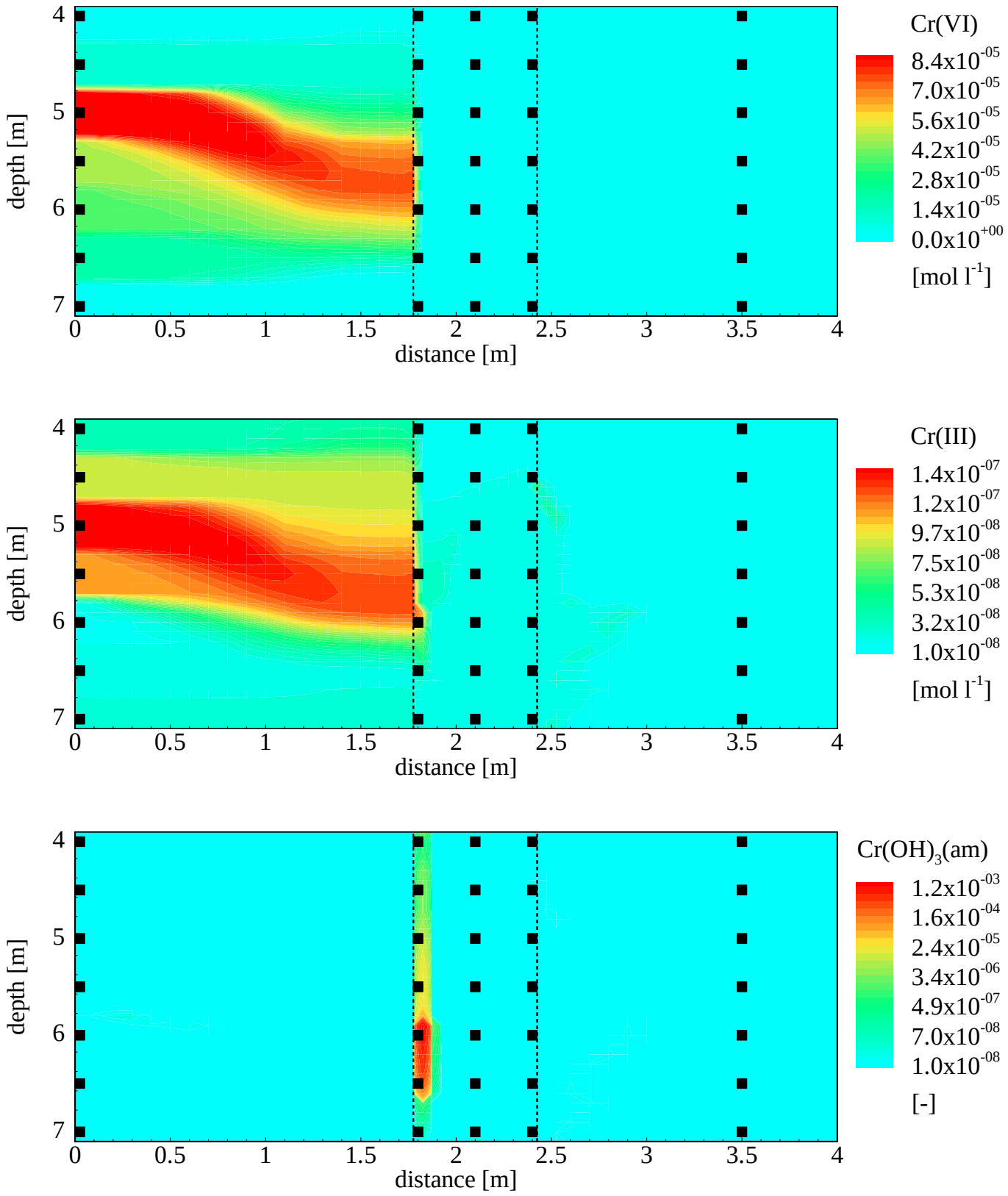

Figure 15. Hexavalent and trivalent chromium concentrations and $CrOH_3$(am) volume fractions after t = 2 years.

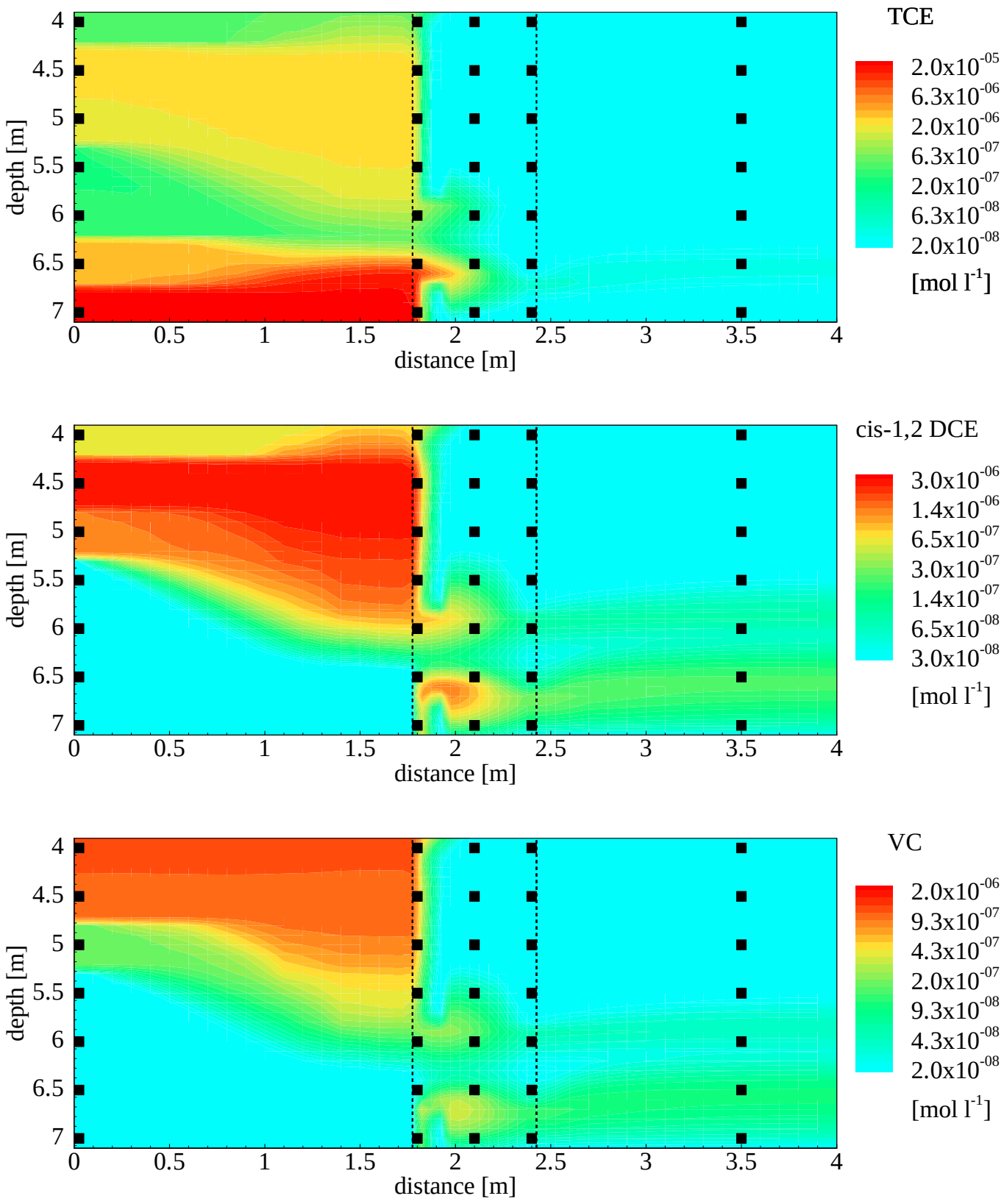

Figure 16. TCE, cis-1,2 DCE and VC concentrations after t = 2 years.

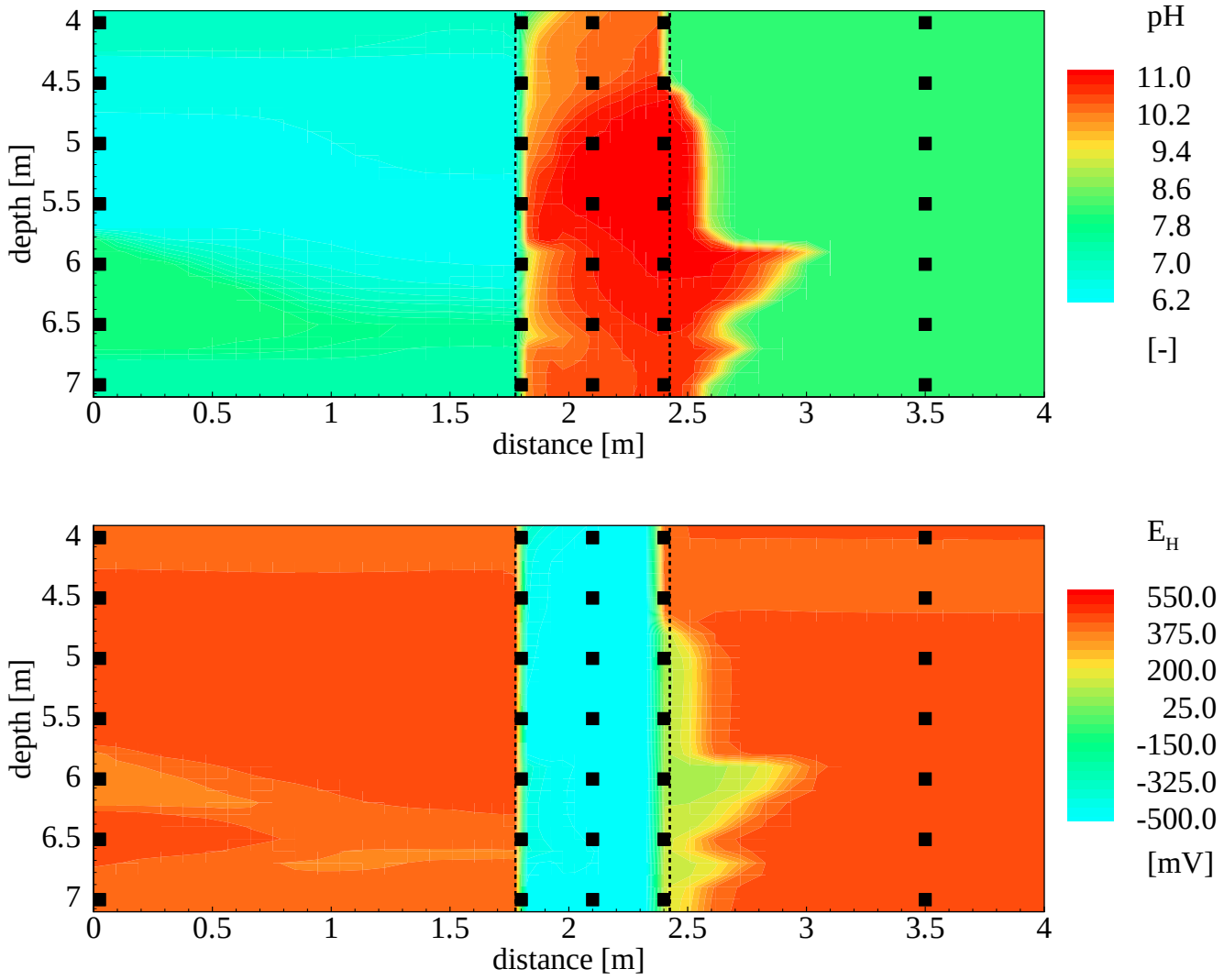

Figure 17. pH and Eh-distribution after t = 2 years.

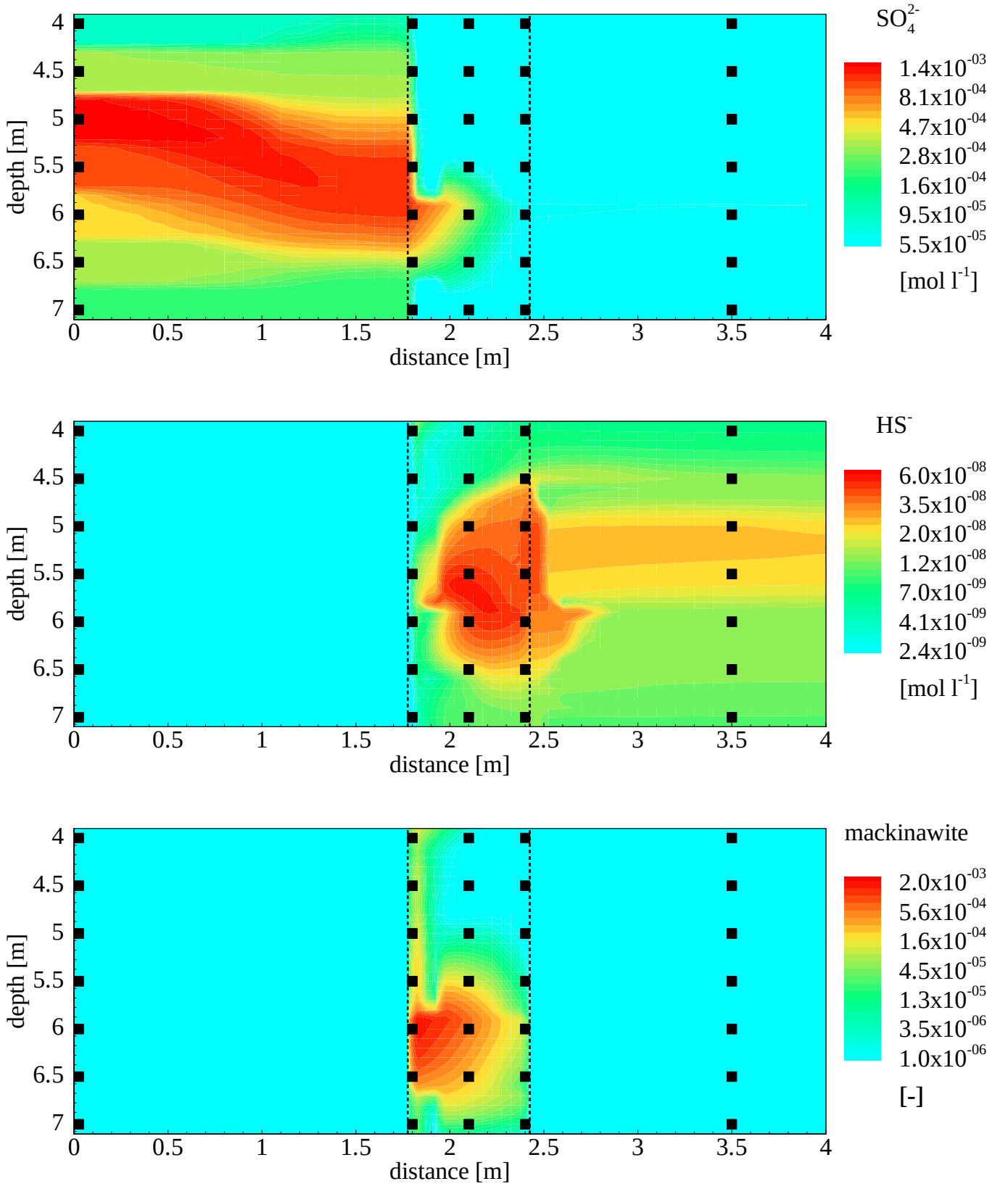

Figure 18. Sulfate and sulfide concentrations and mackinawite volume fractions after t = 2 years.